JOURNAL OF PETROLOGY | VOLUME 48 | NUMBER 2 | PAGES 327–364 | 2007 | doi:10.1093/petrology/egl064

Resetting of the U–Pb Zircon System in Cambro-Ordovician Intrusives of the Deep Freeze Range, Northern Victoria Land, Antarctica

R. M. BOMPAROLA[1]*, C. GHEZZO[1], E. BELOUSOVA[2], W. L. GRIFFIN[2] AND SUZANNE Y. O'REILLY[2]

[1]DIPARTIMENTO DI SCIENZE DELLA TERRA, UNIVERSITÀ DI SIENA, 53100 SIENA, ITALY

[2]GEMOC ARC NATIONAL KEY CENTRE, DEPARTMENT OF EARTH AND PLANETARY SCIENCES, MACQUARIE UNIVERSITY, SYDNEY, NSW 2109, AUSTRALIA

RECEIVED FEBRUARY 25, 2005; ACCEPTED SEPTEMBER 29, 2006;
ADVANCE ACCESS PUBLICATION NOVEMBER 21, 2006

A detailed in situ isotopic (U–Pb, Lu–Hf) and geochemical study of zircon populations in a composite sequence of foliated to massive Cambro-Ordovician intrusions in the Deep Freeze Range (North Victoria Land, Antarctica), has highlighted great complexity in zircon systematics. Zircons in deformed granitoids and tonalites display complex internal textures, a wide spread of concordant U–Pb ages (between 522 and 435 Ma) and unusual trace-element compositions (anomalous enrichment of light rare earth elements, U, Th and Y) within single zircon grains. In contrast, zircons from undeformed samples display a limited range of U–Pb ages and trace-element compositions. Zircons from all age and textural populations in most of the deformed and undeformed samples show a relatively narrow range of ϵ_{Hf} *values, suggesting that the Lu–Hf system remained undisturbed. Inferred emplacement ages cover a time interval of about 30 Myr: from 508 to 493 Ma for the oldest strongly foliated synkinematic Howard Peaks megacrystic monzogranites and high-K calc-alkaline mafic to intermediate rocks of the 'Corner Tonalite' unit; from about 489 to 481 Ma for the younger massive shoshonitic mafic dyke suite and the high-K calc-alkaline Keinath granite. The observed isotopic and chemical variations in zircon are attributed to a sub-solidus recrystallization under hydrous conditions and varying temperature, in a setting characterized by a transpressional to extensional stress regime.*

KEY WORDS: *Antarctica; Cambro-Ordovician intrusives; Ross Orogen; zircon U–Pb geochronology*

INTRODUCTION

Zircon is chemically and physically resistant to modification under most geological conditions; this characteristic makes it one of the most important tools to determine the age, origin and thermal history of crustal igneous and metamorphic rocks. However, many recent studies (e.g. Black *et al.*, 1986; Pidgeon, 1992; Wayne *et al.*, 1992; Vavra *et al.*, 1996, 1999; Pidgeon *et al.*, 1998; Ashwal *et al.*, 1999; Rubatto *et al.*, 1999, 2001; Schaltegger *et al.*, 1999; Hartmann *et al.*, 2000; Hoskin & Black, 2000; Liermann *et al.*, 2002; Rubatto, 2002; Rubatto & Hermann, 2002; Zeck & Whitehouse, 2002; Tomacheck *et al.*, 2003; Whitehouse & Kamber, 2002; Whitehouse & Platt, 2003; Booth *et al.*, 2005; Giacomini *et al.*, 2005) have shown that a high degree of complexity in the internal textures of zircon grains may be associated with disturbance of the U–Pb system in metamorphic and igneous rocks, and often with changes to the chemical composition of the zircons. These studies clearly demonstrate that zircon does not always behave as a closed system. The interpretation of zircon U–Pb ages may therefore contain ambiguities. A number of processes such as igneous and metamorphic overgrowth, inheritance, annealing after radiation damage, hydrothermal alteration, precipitation and dissolution can severely affect the chemical and isotopic systems, leading to mixtures of age

---

*Corresponding author. Telephone: +39-0577233970. Fax: +39-0577 233938. E-mail: bomparola@unisi.it components within single zircon grains. The application of trace-element, U–Pb and Lu–Hf systematics using *in situ* analytical methods [ion-microprobe, laser ablation microprobe–inductively coupled plasma mass spectometry (LA-ICPMS) and multi-collector-LA-ICPMS)] on discrete domains within the same zircon grains has great potential for distinguishing between magmatic, metamorphic and altered zircons. Indeed, the integrated application of these techniques allows correlations between zircon ages, textures, and elemental and isotopic compositions, which are indispensable in dating specific geological events identified in the zircons' growth history.

Many researchers have attributed ambiguity in the interpretation of U–Pb zircon dates principally to partial Pb-loss effects, which result in discordant arrays of radiometric ages. Examples of near-complete Pb loss have been ascribed to extreme processes of mylonitization (Wayne & Sinha, 1988) or leaching of metamict grains by fluids under low-temperature conditions (Gebauer & Grunenfelder, 1976). Recently, several cases of completely reset U–Pb isotopic systems, often accompanied by a redistribution of trace elements, have been described (e.g. Ashwal *et al.*, 1999; Hoskin & Black, 2000; Giacomini *et al.*, 2005).

In this paper we present a detailed *in situ* study of the isotopic (U–Pb and Lu–Hf) and trace-element composition in zircon from nine selected samples of a composite sequence of foliated and massive granitoids and mafic rocks cropping out in the Deep Freeze Range (Northern Victoria Land, Antarctica). The zircons have been analysed by scanning electron microprobe (EMP), LA-ICPMS and MC-LA-ICPMS.

Previous studies of the Wilson Terrane in the Northern Victoria Land constrain the age of intrusive magmatism to between 530 and 480 Ma (Armienti *et al.*, 1990; Tonarini & Rocchi, 1994). However, the intrusive sequence in the Deep Freeze Range is still poorly constrained. Published Rb/Sr whole-rock–biotite pairs and K/Ar data on biotite from both metamorphic and magmatic rocks cropping out in the study area give younger ages between 475 and 449 Ma, which are interpreted as cooling ages (Borsi *et al.*, 1987; Kreuzer *et al.*, 1987; Vita *et al.*, 1991). In addition, the Deep Freeze Range area was affected, during the Ross Orogeny, by ductile deformational events triggered by dextral strike-slip and/or reverse shear zones and several minor local shear bands (Skinner, 1991; Musumeci & Pertusati, 2000). In most of the studied rocks, shearing and deformation produced a pervasive solid-state ductile high-temperature deformation and recrystallization of the magmatic minerals and probably favoured a strong interaction with fluids, as suggested by a common pervasive presence of fluid inclusions. The wide spectrum of U–Pb ages and trace-element compositions in the zircons of some samples indicates that in such a setting, the isotopic and compositional systematics of zircon underwent a strong modification.

This study of zircon populations in selected plutonic rocks focuses on the relationships between syn- and post-magmatic events and the partial resetting of the U–Pb and trace-element chemistry of the zircons. Hf isotopes provide an invaluable tracer in this type of study; they make it possible to unravel the complex history of the zircon populations and help to identify multiple age components.

GEOLOGICAL BACKGROUND

During Late Proterozoic–Early Palaeozoic time, active subduction was occurring along the palaeo-Pacific margin of the East Antarctic Craton. This subduction generated the Late Cambrian–Early Ordovician Ross–Delamerian Orogen, a 4000 km long mobile belt, now exposed on the border of the East Antarctic Craton and in South Australia (Stump, 1995; Goodge, 2002; Goodge *et al.*, 2004a, 2004*b*; Wysoczanski & Allibone, 2004, and references therein). The Transantarctic Mountains, generated by uplift of the craton-ward shoulder of the Cretaceous–Cenozoic rift, broadly parallel the older Ross Orogen and expose the crystalline basement.

In Northern Victoria Land (NVL) cratonward-directed subduction resulted in the accretion of the exotic Bowers and Robertson Bay Terranes to the inboard Wilson Terrane, which then represented the early Palaeozoic active margin of the East Antarctic Craton (Bradshaw & Laird, 1983; Kleinschmidt & Tessensohn, 1987; Kleinschmidt *et al.*, 1992; Matzer, 1995; for an updated discussion of the tectonic architecture of the NVL, see Roland *et al.*, 2004; Tessensohn & Henjes-Kunst, 2005). In the Wilson Terrane these accretionary processes generated a wide fold–thrust metamorphic belt and widespread syn-, late- and post-tectonic plutonism between about 530 and 480 Ma (Armienti *et al.*, 1990; Tonarini & Rocchi, 1994, and references therein) represented by the Granite Harbour Intrusives (Gunn & Warren, 1962; Borg *et al.*, 1987; Vetter & Tessensohn, 1987; Armienti *et al.*, 1990; Fenn, 1993; Schüssler *et al.*, 1993; Olesch *et al.*, 1996). The intrusive rocks include both I-type metaluminous and S-type peraluminous calc-alkaline magmas, with variable K enrichment and magmatic arc affinity (Borg *et al.*, 1987; Ghezzo *et al.*, 1987; Vetter & Tessensohn, 1987; Armienti *et al.*, 1990; Biagini *et al.*, 1991*a*, 1991*b*; Di Vincenzo & Rocchi, 1999; Dallai *et al.*, 2003; Rocchi *et al.*, 2004). The metamorphic rocks intruded by the GHI can be subdivided into an eastern medium- to high-pressure belt including ultrahigh-pressure eclogitic lenses, and a western low- to medium-pressure–high-temperature belt that is locally in granulite facies (Grew *et al.*, 1984; Talarico & Castelli, 1995; Di Vincenzo *et al.*, 1997; Schüssler *et al.*, 2004; Talarico *et al.*, 2004, and references therein).

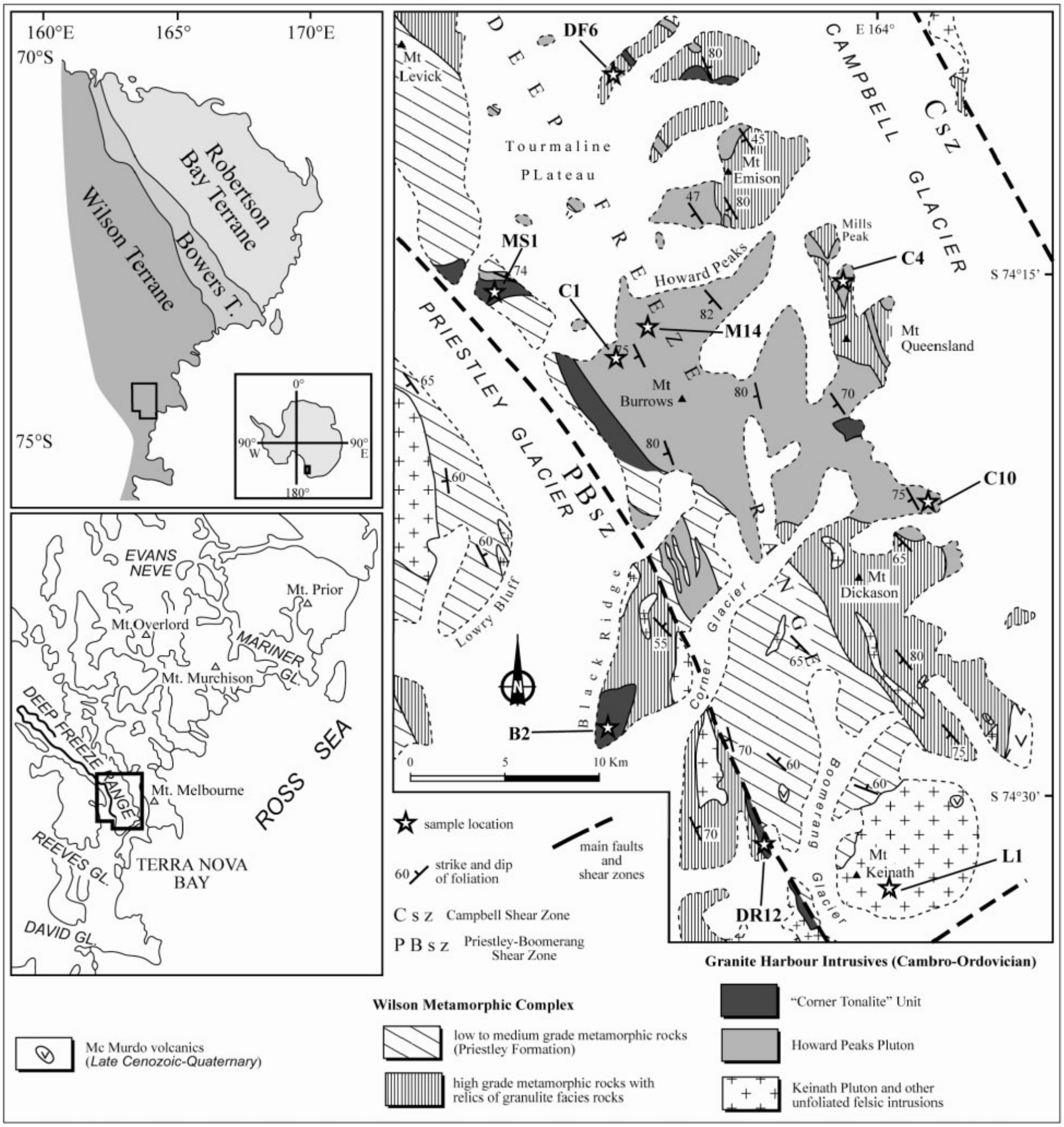

Fig. 1. Geological map of the Deep Freeze Range, Northern Victoria Land, Antarctica [modified after Musumeci & Pertusati (2000)].

In the Deep Freeze Range (Fig. 1), an intermediate belt of the Wilson Terrane, a complex sequence of metaluminous and peraluminous granitoids and mafic intrusive rocks is well exposed and here defined as the Deep Freeze Range Intrusive Complex (DFRIC). Magmatic rocks include plutons and satellite plugs of variable size and degree of foliation, and dyke swarms. Mapping in the Mt. Levick–Browning Pass region has identified four distinct intrusive units: (1) foliated coarse-grained inequigranular granitoids (the Howard Peaks Pluton); (2) a foliated medium-grained gabbro–tonalite–granodiorite sequence (the 'Corner Tonalite', Adamson, 1971); (3) unfoliated biotite monzogranites (the Keinath Pluton, Skinner, 1983) and granodiorites; (4) a widespread complex of fine-grained felsic and mafic dykes and of aplite–pegmatites that crosscut the whole basement. The metamorphic country rocks have a complex history characterized by a low- to high-grade metamorphism (with remnants of a

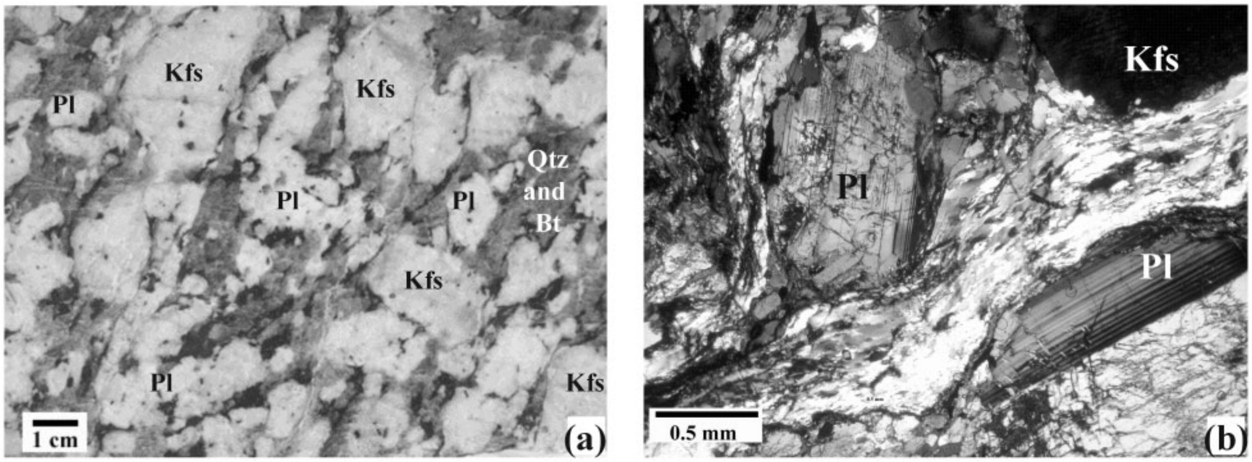

Fig. 2. (a) Ductile deformation fabric in a foliated porphyritic Howard Peaks granitoid (sample Cl, polished slab). (b) Photomicrograph (crossed Nicols) of a typical medium-strain fabric in deformed porphyritic Howard Peaks granite (sample Cl) showing fine-grained recrystallized elongated aggregates of quartz and minor biotite surrounding plagioclase porphyroclasts.

granulite-facies complex, Talarico & Castelli, 1995) of low-pressure type with contrasting P–T–t paths (Palmeri, 1997; Talarico *et al.*, 2004, and references therein).

For this study nine samples from the Howard Peaks Pluton, the 'Corner Tonalite' unit, the Keinath Pluton and the unfoliated mafic dyke swarm have been selected.

The Howard Peaks Pluton (HPP; Fig. 1) is the largest intrusion in the region and is a composite pluton. It occurs in scattered outcrops over an area of about 200 km^2 between the eastern side of the Priestley Glacier and the Campbell Glacier, in and south of the Tourmaline Plateau. The HPP is composed of dominant coarse-grained porphyritic biotite monzogranites (Fig. 2a) with 5–8 cm K-feldspar megacrysts and rare mafic microgranular enclaves, and minor granodiorites. The HPP corresponds to the 'Dickason Granite' of Adamson (1971), but Ghezzo *et al.* (1987) referred to these rocks as the HPP because Mt. Dickason comprises unrelated migmatitic rocks.

Intrusive contacts with the medium- to high-grade metamorphic country rocks are sharp and often subvertical. A marked magmatic foliation that dips 60°–80° toward the SW, parallel to the NW–SE-striking regional S_2 schistosity, is developed throughout the HPP. This foliation is defined by the preferred orientation of magmatic minerals. A high- to moderate-temperature solid-state ductile deformation is common and often produces an augen-gneiss fabric superimposed on the magmatic fabric; this fabric is more pronounced along discrete shear bands that strike NW–SE. All structural criteria such as deformation and rotation of the feldspar megacrysts (Passchier & Trouw, 2005) are consistent with a dextral sense of shear.

Preliminary chemical and isotopic analyses (unpublished data) indicate that HPP monzogranites are metaluminous, with SiO_2 and K_2O contents in the range 68–74% and 5–6%, respectively, high values of large ion lithophile element to high field strength element ratio (LILE/HFSE), a negative Nb–Ta anomaly and Rb/Sr ratios around two. High $^{87}Sr/^{86}Sr$ ratios at 500 Ma, in the range 0·710–0·716, suggest a crustal origin. The HPP monzogranites share many characteristics with the Abbott Granite in the Northern Foothills (Skinner, 1983; Armienti *et al.*, 1990; Di Vincenzo & Rocchi, 1999), an intrusive unit with a high-K shoshonitic affinity, and with the DV2 monzonitic suite from the Dry Valleys region in southern Victoria Land (Allibone *et al.*, 1993*a*, 1993*b*; Cox *et al.*, 2000).

The 'Corner Tonalite' (CT; Fig. 1) is a mafic complex mainly cropping out along Black Ridge and the eastern side of the Priestley Glacier. Dominant tonalites ['Corner Tonalite' of Adamson (1971)] and quartz diorites are accompanied by minor gabbro and ultramafic rocks. The relatively mafic rocks are locally interlayered with sheets of granodiorite and monzogranite near the margins of the HPP. The rocks are subalkaline with a dominant high-K calc-alkaline affinity. All these intrusives commonly display a steeply dipping NW–SE-striking foliation parallel to the metamorphic foliation in the adjacent country rocks. The foliation is generally magmatic in origin, but along discrete shear bands is commonly overprinted by a solid-state deformation fabric. Where in contact with the Howard Peaks Pluton, the CT shows field evidence of mixing processes that gave rise to a heterogeneous granodioritic facies with large rounded K-feldspar megacrysts.

The Keinath Pluton (KP) is a large (about 50 km^2) relatively homogeneous pluton composed of massive equigranular medium-grained biotite monzogranites with abundant mafic microgranular enclaves. Other smaller bodies of similar granitoids crop out in the Cape Sastrugi–Boomerang Glacier area. Petrographic and chemical data (Armienti *et al.*, 1990, and unpublished data) indicate a metaluminous high-K calc-alkaline character similar to the dominant I-type suite in the Wilson Terrane (Borg *et al.*, 1987; Armienti *et al.*, 1990) and to the DV1a suite from the Dry Valleys region (Allibone *et al.*, 1993*b*; Cox *et al.*, 2000).

The dyke complex is a composite and not cogenetic complex.

Felsic dykes are fairly common, particularly in the medium- to high-grade and granulite-facies metamorphic rocks. Both foliated and unfoliated dykes are present (Musumeci & Pertusati, 2000).

Foliated felsic dykes are mainly represented by peraluminous two-mica ± garnet ± andalusite ± cordierite leucogranites and monzogranites showing concordant (sheet intrusions) or discordant contacts with the metamorphic rocks, sometimes folded, and commonly emplaced along the S_2 foliation ('Synkinematic Peraluminous Leucogranites', Biagini *et al.*, 1991*a*). Foliation is related to moderate-temperature solid-state deformation (Musumeci & Pertusati, 2000).

Unfoliated felsic dykes and stocks are common in the metamorphic rocks, typically as satellite plugs of the major plutons. They are equigranular or sometimes porphyritic, fine- to medium-grained metaluminous biotite monzogranites and granodiorites. Undeformed garnet–tourmaline-bearing aplite–pegmatitic veins and dykes crosscut all the basement rocks; they are particularly common in the granulite-facies rocks.

Unfoliated mafic dykes appear as phenocryst-poor, fine-grained massive dark rocks, lacking evidence of deformation. They are mainly microdiorites, quartz microdiorites and microtonalites. The geochemistry of these mafic rocks is characterized by a dominant high-K shoshonitic affinity and trace-element patterns similar to those of the mafic facies of the Vegetation Unit in the Terra Nova Intrusive Complex (Rocchi *et al.*, 2004). All these fine-grained unfoliated rocks show textures that suggest a shallow tensional emplacement regime.

The emplacement of the intrusive sequence in the Deep Freeze Range has been described by Musumeci & Pertusati (2000): a mainly synkinematic emplacement is proposed for most of the intrusive bodies. They were intruded into low- to high-grade metamorphic rocks exploiting orogen-parallel thrust faults and transpressional structures controlled by two major ductile shear zones that run along the Priestley–Boomerang Glaciers and the Campbell Glacier [see also Läufer & Rossetti (2003) and references therein]. These shear zones have been reactivated in Cenozoic time (the 'Priestley Fault' and 'Campbell Fault') by a regional strike-slip fault system (Salvini *et al.*, 1997; Storti *et al.*, 2006). The Howard Peaks Pluton was emplaced in a push-up zone, as indicated by the sigmoidal pattern of magmatic foliation and the asymmetric shape with tails parallel to the shear zones (Musumeci & Pertusati, 2000). Some bodies of the 'Corner Tonalite' unit and many dykes, particularly some peraluminous felsic leucogranites, were also involved in the shear deformation. The emplacement depth of the intrusive sequence is poorly defined: preliminary data from the Al-in-hornblende geobarometer (Anderson & Smith, 1995) suggest an emplacement pressure of about 4 GPa for the CT. Furthermore, the timing of the magmatic and structural events detailed above is poorly constrained.

Previous studies indicated an age of 481 ± 10 Ma (Rb/Sr whole-rock isochron) for peraluminous synkinematic dykes in the Deep Freeze Range (Tonarini & Rocchi, 1994). Rb/Sr whole-rock–biotite ages, and K/Ar ages on biotite (Borsi *et al.*, 1987; Kreuzer *et al.*, 1987; Vita *et al.*, 1991) on samples from the Howard Peak Pluton, the 'Corner Tonalite' and some metamorphic rocks from Mt. Emison in the Deep Freeze Range (including a granulite), indicate cooling ages in the range 475–449 Ma.

ANALYTICAL METHODS

To collect a representative zircon population, about 1–2 kg of each sample was processed using a disc mill, shaking table, Frantz magnetic separator and heavy liquids. Representative crystals (about 100 grains) of different morphology and colour were then hand-picked from the final mineral separate, mounted in 25 mm epoxy discs and polished. A CAMEBAX SX50 electron microprobe at the ARC National Key Centre for the Geochemical Evolution and Metallogeny of Continents (GEMOC) was used to analyse the major constituents of zircons (Zr and Si) and selected minor elements (Hf, Y, U and Th), as well to image the internal zoning pattern of the crystal sections using a backscattered electron (BSE) detector. The BSE detector is a light-sensitive diode; when operated at appropriate conditions, it produces images of zircon texture that reflect both variations in the mean atomic number and the cathodoluminescence (BSE/CL images). Operating conditions for the EMP were 15 kV accelerating voltage and a beam current of 20 nA. The sample mounts were cleaned, together with zircon standards, in 2N nitric acid for *c.* 1 h to remove surface Pb contamination. Zircons were analysed for U, Th and Pb isotopic compositions using two LAMs (266 and 213 nm) attached to an Agilent 4500 series 300 ICPMS system at GEMOC. Samples and standards were ablated in a custom-built sample chamber using He as carrier gas. The ablation in He, rather than Ar, minimizes deposition of ablation products around ablation sites, improves sample transport efficiency, and gives more stable signals and more reproducible U–Pb fractionation (Jackson *et al.*, 2004). All analyses were performed with the laser focused above the sample (typically 150–250 μm) to minimize dynamic U–Pb fractionation as the laser beam penetrates into the sample

(Hirata & Nesbitt, 1995). Constant LAM operating conditions were maintained throughout each run of 20 analyses to ensure constant U–Pb fractionation. Samples and standards were analysed in runs of 20 analyses, including 12 unknowns and eight analyses of the GEMOC/GJ-1 zircon standard (609 Ma). The unknowns included two near-concordant standard zircons, 91500 and Mud Tank, which were analysed in each run as an independent control on reproducibility and instrument stability. Each analysis lasted about 180 s, with gas background measurements being taken over the first 60 s, prior to initiation of ablation. The signals of masses ^{206}Pb, ^{207}Pb, ^{208}Pb, ^{232}Th and ^{238}U were acquired using the instrument's time-resolved analysis data acquisition software. ^{204}Pb was not measured, because of the low count rates and the isobaric interference from Hg that is a contaminant of the Ar supply gas. ^{235}U was calculated from the ratio $^{235}\text{U} = {}^{238}\text{U}/137{\cdot}88$. Raw data were processed using GLITTER, an in-house data reduction program (van Achterbergh *et al.*, 2001). Identical integrated ablation time segments for each sample and standard zircon were selected, thus correcting for the effects of laser-induced fractionation. The contents of common lead were estimated from the three-dimensional discordance pattern in ^{206}Pb/^{238}U–^{207}Pb/^{235}U–^{208}Pb/^{232}Th space and corrected accordingly (Andersen, 2002). Concordia ages were determined using Isoplot 2.32 (Ludwig, 1999). Further details of the analytical technique, instrumental conditions and measurement procedures have been given by Belousova *et al.* (2001) and Jackson *et al.* (2004). The precision (1σ) of the method (using a spot size of 40 μm and a pulse energy of 0·25 mJ) evaluated on the GJ-1 zircon is close to 1% for the ^{206}Pb/^{238}U and ^{207}Pb/^{235}U ratios. Some age measurements were also performed using a 213 nm laser ablation microprobe, coupled to a magnetic sector ICP-MS at CNR–Istituto di Geoscienze e Georisorse of Pavia, Italy. Ablation of samples and standards was performed in an in-house built ablation cell, using He as the carrier gas and 91500 zircon (1065 Ma) as external standard. The signals of masses ^{206}Pb, ^{207}Pb, ^{235}U and ^{238}U were acquired in magnetic scan mode (B-scan) at a spatial resolution of 40 μm. Accuracy ranges between 1% and 5% and is strictly related to Pb content in zircon. Details of the analytical technique, experimental conditions, data accuracy and precision have been given by Tiepolo (2003).

Trace-element concentrations were obtained on zircons from seven of the selected samples using the LA-ICPMS system at CNR–Pavia. NIST-610 was used as an external standard to correct for mass bias and laser-induced elemental fractionation. The data were normalized for each analysis to the electron microprobe Zr concentration as an internal standard. Precision and accuracy are generally better than 10%, and limits of detection are down to the ppb level for the heaviest elements. A detailed description of the method has been given by Tiepolo *et al.* (2002).

Hf isotope analyses for the same set of zircons were carried out *in situ* using two New Wave/Merchantek laser ablation microprobes (193 nm, 213 nm), attached to a Nu Plasma MC-ICPMS system at Macquarie University, Sydney. Operating conditions were 10 Hz repetition rate and energies of 0·6–1·3 mJ/pulse for the 213 nm laser, and 2 Hz repetition rate and energies of 0·03–0·05 mJ/pulse for the Excimer (193 nm) laser. Typical ablation times were 80–120 s, resulting in pits of 40–60 μm and 30–40 μm deep with the 213 and 193 nm lasers, respectively. The methods and analyses of standard solutions and standard zircons have been described by Griffin *et al.* (2000). Helium was used as carrier gas to transport the ablated sample from the laser-ablation cell to the ICPMS torch, via a mixing chamber. The masses analysed for this work are 172, 175, 176, 177, 178, 179 and 180. Analyses were carried out in static-collection mode and all masses acquired simultaneously in Faraday cups. Data were normalized to $^{179}\text{Hf}/^{177}\text{Hf} = 0{\cdot}7325$, using an exponential correction for mass bias. Interference of ^{176}Lu on ^{176}Hf was corrected by measuring the intensity of the interference-free ^{175}Lu isotope and using the recommended $^{176}\text{Lu}/^{175}\text{Lu} = 0{\cdot}02669$ to calculate ^{176}Lu/^{177}Hf. Interference of ^{176}Yb on ^{176}Hf was corrected by measuring the interference-free ^{172}Yb isotope and using ^{176}Yb/^{172}Yb to calculate ^{176}Yb/^{177}Hf. The appropriate value of $^{176}\text{Yb}/^{172}\text{Yb} = 0{\cdot}5865$ was determined by successively spiking the JMC475 Hf standard (1 ppm solution) with Yb, and iteratively finding the value of ^{176}Yb/^{172}Yb required to yield the value of ^{176}Hf/^{177}Hf obtained on the pure Hf solution. The measured ^{176}Lu/^{177}Hf ratios were then used to calculate initial ^{176}Hf/^{177}Hf ratios. The typical uncertainty on a single analysis of ^{176}Hf/^{177}Hf is ±0·000020, equivalent to an uncertainty of less than one epsilon unit. Mud Tank and 91500 standards were used to check the accuracy and precision of the laser-ablation results within each run.

All analyses were performed directing the laser to specific textural domains and avoiding mixed textural domains and mineral inclusions in the zircon grains.

SAMPLE CHARACTERISTICS

Zircon crystals were analysed from four samples (M14, C1, C10, DF6) selected to be representative of the major foliated porphyritic biotite monzogranitic facies, one sample (C4) of the foliated porphyritic biotite granodiorite from Mills Peak, all from the Howard Peaks Pluton; two samples are a foliated quartz diorite and a tonalite (B2 and MS1) from the 'Corner Tonalite' unit; one sample (L1) is a massive biotite monzogranite from the Keinath Pluton; and one is a pyroxene micro-monzodiorite

(DR12) from the unfoliated mafic dyke swarm. Locations are given in Fig. 1.

The nine studied samples show different fabrics: M14, C1, C10, DF6, C4 and MS1 show both magmatic foliation and solid-state ductile deformation. Deformation is more pronounced in DF6 and C4, and moderate in MS1. Sample B2 is characterized only by a magmatic foliation. Samples L1 and DR12 are massive. Sample codes, localities and latitude and longitude are given in the Appendix.

Howard Peaks Pluton

Samples M14, C1 and C10 are typical coarse-grained, foliated, megacrystic, biotite monzogranites characterized by the following main mineral phases: variable amounts of perthitic microcline (mainly as 2–8 cm megacrysts), zoned plagioclase (28–42% An), quartz, biotite ($X\text{Mg} = 0{\cdot}35$–$0{\cdot}45$) (Fig. 2b); apatite, allanite, ilmenite, monazite, rutile and zircon are common accessory phases. Sample DF6 is a foliated porphyritic monzogranite from the eastern border of the Howard Peaks Pluton. It is petrographically similar to the main monzogranites, but it is a relatively low-silica facies (around 70% SiO_2) and contains small amounts of orthopyroxene and slightly higher amounts of biotite. In these rocks deformation and partial recrystallization of the magmatic minerals has produced elongate fine-grained stringers of quartz, plagioclase and biotite that wrap around K-feldspar and plagioclase grains, myrmekite along the margins of igneous K-feldspar, ductile deformation of quartz to form ribbons or aggregates of new grains, and bending of plagioclase crystals, all features consistent with a high- to moderate-temperature solid-state deformation (Paterson *et al.*, 1989; Tribe & D'Lemos, 1996). The common occurrence of 'chessboard' subgrain patterns in quartz confirms the high P–T conditions of deformation (Kruhl, 1996). Trails of fluid inclusions, with a variable composition (often CO_2-rich), are common in quartz.

Sample C4 is a foliated porphyritic biotite granodiorite with plagioclase and K-feldspar megacrysts, from a stock intruded in the granulite-facies metamorphic rocks at Mills Peaks. In this sample a postkinematic annealing event is overprinted on the gneissic fabric and is characterized by a fine-grained polycrystalline aggregate, lacking evidence of strain and interposed between the feldspar megacrysts. The sample from this outcrop has been included in the HPP, because of its striking fabric similarity to the typical megacrystic monzogranites of the HPP. However, preliminary chemical and isotopic data suggest that it probably belongs to a local, not cogenetic intrusion, coeval with the main HPP.

'Corner Tonalite'

Samples MS1 and B2 are two foliated hornblende–biotite-bearing plutonic rocks (a tonalite and a quartz diorite) outcropping at the western side of the Howard Peaks intrusion and at Black Ridge, respectively. MS1 is characterized by a pervasive overprinted solid-state deformation; B2 shows no evidence of post-crystallization deformation. They are medium-grained rocks with a colour index of about 30, with abundant green hornblende and minor brown biotite. Plagioclase is strongly zoned and ranges in composition from andesine to labradorite; quartz is interstitial; accessory minerals are apatite, sphene, magnetite and zircon. A few trails of small fluid inclusions occur mainly in sample MS1.

Keinath Pluton

Sample L1 is a massive equigranular medium-grained biotite monzogranite. Plagioclase is a strongly zoned andesine, K-feldspar is a perthitic microcline; accessory minerals are apatite, sphene, magnetite and zircon. The presence of minor epidote and chlorite suggests a moderate subsolidus alteration; a few fluid inclusion trails occur locally in quartz.

Mafic dyke swarm

Sample DR12 is a fine-grained undeformed massive phenocryst-poor (plagioclase) micro-monzodiorite dyke from the western side of the Boomerang Glacier, intruded within strongly foliated and deformed granitoids. It is characterized by dominant euhedral zoned plagioclase (33–48% An), quartz and rare interstitial orthoclase; the mafic phases are biotite, orthopyroxene and clinopyroxene. Apatite is abundant as needles; sphene, zircon and ilmenite are common accessory phases.

ZIRCON TEXTURES AND U–Pb RESULTS

Howard Peaks Pluton

Porphyritic biotite monzogranites (samples M14, C1, C10)

Abundant zircon grains are distributed throughout these samples and commonly are included in the main mineral phases (quartz, feldspar and biotite); they also occur in recrystallized areas. They range in length between about 400 and 50 μm and show variable amounts of apatite and fluid inclusions.

BSE/CL images (Fig. 3a–j) reveal a wide spectrum of internal textures in zircon, not always readily interpretable as primary. Most of the investigated crystals show oscillatory zoning defined by variable degrees of thickness and brightness. Three main groups of textures have been distinguished, which characterize individual domains within zircon grains or the whole grains: fine-scale oscillatory zoning, thick zoning and complex zoning. Fine-scale oscillatory zoning is characterized by thin zones showing low contrast in brightness; thick zoning is defined by thick bright bands alternating with darker zones; complex zoning includes a variety of textures

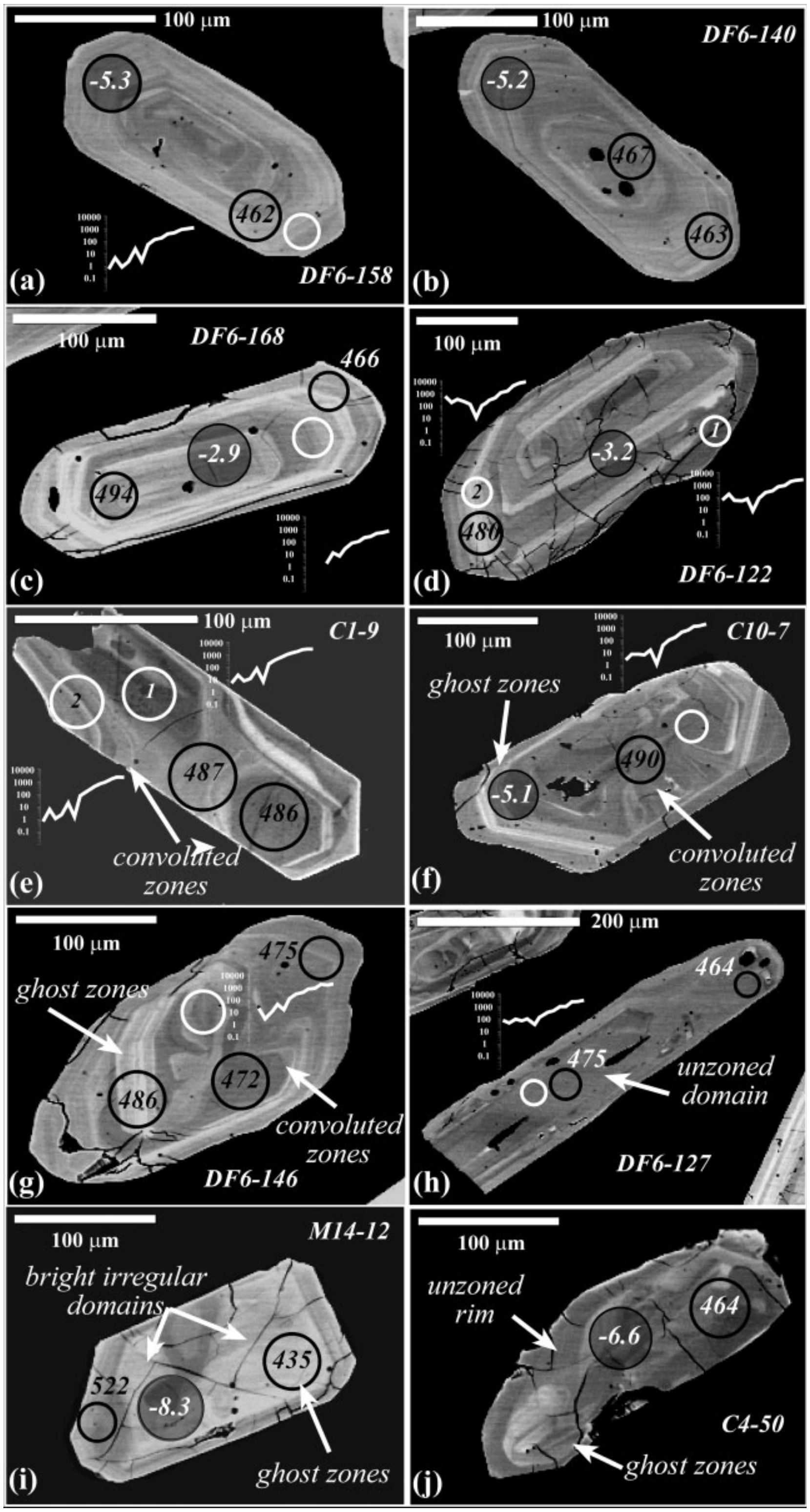

Fig. 3. Backscattered/cathodoluminescence images of representative internal textures of zircons from the monzogranitic and granodioritic samples C1, C10, M14, DF6, C4. Black, white and filled grey circles are locations of U–Pb, trace-element and Lu–Hf LA-ICPMS analyses, respectively. Crystal and shot numbers correspond to those given in Tables 1, 2 and 4. ^{207}Pb/^{206}Pb concordant ages, ϵ_{Hf} values and REE patterns are also indicated. (a)–(c) zircons characterized by fine-scale oscillatory zoning; (d) bright thick zones; (e)–(j) complex textures characterized by: convoluted zones (e)–(g); bright irregular domains (i); ghost zones (f), (g), (i), (j); unzoned rims (j); unzoned zircon domains (h).

and covers the majority of the grains. Complex textures include alternating convoluted bands distinguished by different BSE/CL intensity, which sometimes preserve ghosts of oscillatory zoning, and unzoned patches with or without small bright patches in BSE/CL images.

U–Pb results are shown in Fig. 4a–f. Selected U–Pb data are listed in Table 1. The complete dataset is provided as Electronic Appendix 1, available for downloading from http://www.petrology.oupjournals.org. The concordia and weighted average ages are shown at the 95% confidence level. To construct the weighted average age and the probability density plots concordant $^{207}Pb/^{206}Pb$ ages as calculated by Isoplot 2.32 (probability of concordance >0·001) were used (Ludwig, 1999).

In all the analysed samples there is a relationship between texture and the degree of concordance of the U–Pb ages: the domains characterized by thick zoning often show discordant ages.

Inherited components are also often present. They occur mainly as relict cores with different textures, size and morphology; these are not shown in the U–Pb diagrams nor discussed in this paper.

Sample M14 is characterized by a wide scatter of concordant U–Pb ages, between 522 and 435 Ma (Fig. 4a and Table 1). The probability density plot (Fig. 4b) of the concordant ages shows many peaks without clear gaps between them. The spread in concordant ages may be related to a relatively short time interval between the magmatic intrusion and a discrete resetting event. Therefore, the whole U–Pb dataset cannot be here used to infer the emplacement age of the granite; most of the young ages do not reflect the primary magmatic age but represent varying degrees of incomplete or complete resetting of the primary undisturbed igneous zircons. The oldest peak in the probability density plot (Fig. 4b) therefore is used to infer the magmatic age: nine analyses with a mean age of 506 ± 7 Ma (MSWD = 2); the 20 younger ages ranging between 488 and 435 Ma represent reset ages.

In sample C1, U–Pb ages range from 508 to 472 Ma (Table 1, Fig. 4c). In the probability density plot (Fig. 4d), concordant ages define two main peaks. The oldest peak of 18 points with weighted average ages of 499 ± 2·4 Ma (MSWD = 1·3) represents the emplacement age of the sample. A younger peak of 12 points around 484 Ma (Fig. 4d) and a single spot at 472 Ma reflect Pb loss. A relationship between age populations and textural domains is not obvious; the older ages were measured on differently zoned domains (oscillatory and complex zoning).

In sample C10 (Fig. 4e and Table 1) many discordant data (11 analyses) are present, making it difficult to recognize a primary age or a subdivision into different age populations. The relatively large scatter in the Tera–Wasserburg diagram (Fig. 4e) suggests that the data are probably affected by both an uncorrected common lead component and Pb loss. The few concordant data (22) scatter between 505 and 455 Ma (Fig. 4e); the oldest 12 analyses define a peak around 493 ± 3·8 Ma at 95% confidence (MSWD = 1·3) (Fig. 4f). The older ages are found in zircons showing different textural features: zoned and unzoned domains, and resorbed cores showing convoluted zones. Younger concordant ages between 481 and 455 Ma have been measured on unzoned or weakly zoned domains.

Porphyritic orthopyroxene-bearing monzogranite (sample DF6)

The large number (42 grains) of zircons selected from sample DF6 show grain sizes and morphological features similar to those described for the zircons extracted from the other granitic samples. Inclusions of apatite and fluids are common. As shown in the concordia plot (Fig. 5a), most data (43 of 53 analyses) plot along concordia, defining a wide range of ages between 501 and 448 Ma (Table 1). The probability density plot (Fig. 5b) for the concordant data alone shows three main peaks. The oldest peak defines a plateau around 498 ± 6·6 Ma (four analyses) (MSWD = 1·3; Fig. 5b), but most of the analyses (39) show relatively 'young' ages. No systematic variations can be observed between zoned and unzoned or complexly zoned crystals, but most of the domains characterized by thick zoning and bright-BSE/CL patches show slightly discordant ages.

Porphyritic biotite granodiorite (sample C4)

Zircons recovered from sample C4 show the same range of textural features and size displayed by the Howard Peaks samples, but with a predominance of domains characterized by complex zoning (Fig. 3j). Fluid inclusions are abundant and apatite inclusions are also present. Crystal shapes vary from elongated and prismatic to anhedral. Oscillatory zoning is common and can either include the entire zircon texture or occur in rims around unzoned or more complexly zoned cores. Bright domains are often present as cores or patches distributed throughout the crystal. Zircons showing oscillatory zoning often display bright thick zones. Finally, more complex features such as internal convoluted surfaces are widespread. Inherited cores, highly variable in size and shape, are also present. They are typically surrounded by weakly zoned or unzoned rims, separated by planar or rounded surfaces with bright bands sometimes present at the core–rim boundary. Textureless inherited grains are also present.

U–Pb results (Table 1, Fig. 5c and d) show a broad spectrum of zircon ages for this sample. No relationship exists between zircon age and morphology, and a subdivision into different age groups based on BSE/CL images is difficult. Concordant ages (Fig. 5c) range from 506 to

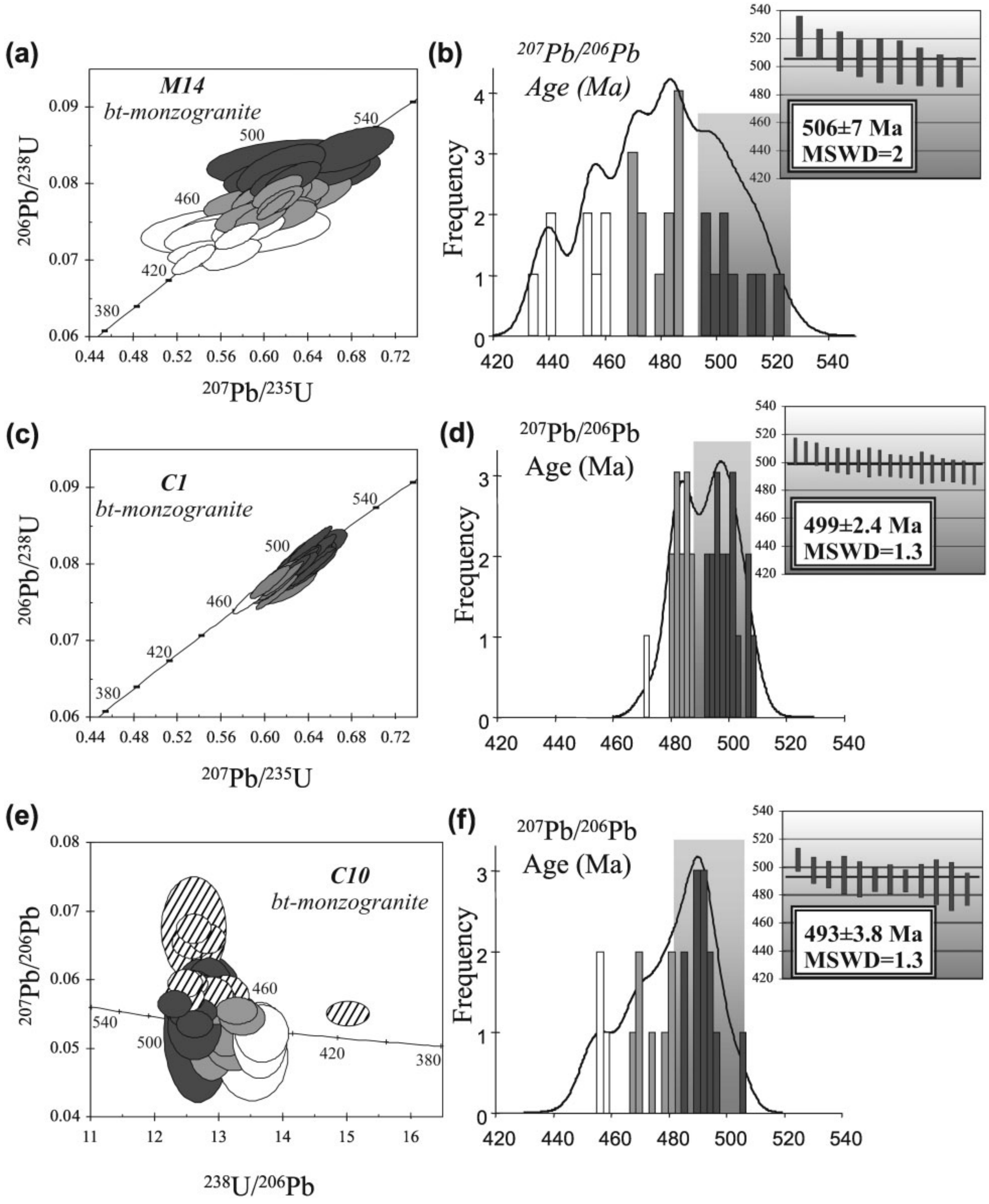

Fig. 4. Isotope ratio plots (concordia and inverse concordia diagrams) (a), (c), (e), and probability density plots and weighted average ages (b), (d), (f) of LA-ICPMS U–Pb data for zircons from the Howard Peaks monzogranitic samples. Error ellipses and bars are given at 2σ level. Dark and light grey, and white ellipses and bars are concordant 'age populations'; diagonally shaded ellipses are discordant data, not shown in the weighted average and probability density plots.

Table 1: Representative LA-ICPMS U–Th–Pb isotopic data and calculated ages for zircons from theDeep Freeze Range intruvives

Sample	f_{206} (%)	Isotopic ratios								Ages							
		^{207}Pb/ ^{206}Pb	RSD	^{207}Pb/ ^{235}U	RSD	^{206}Pb/ ^{238}U	RSD	^{208}Pb/ ^{232}Th	RSD	^{207}Pb/ ^{206}Pb	1σ	^{207}Pb/ ^{235}U	1σ	^{206}Pb/ ^{238}U	1σ	^{208}Pb/ ^{232}Th	1σ
C1, Howard Peaks bt-monzogranite																	
C1-8 fz		0·0565	1·15	0·6064	1·23	0·0778	1·12	0·0225	1·34	473	26	481	5	483	5	449	6
C1-9.1 c		0·0568	1·25	0·6141	1·34	0·0785	1·16	0·0229	1·18	483	28	486	5	487	5	457	5
C1-9.2 c		0·0569	1·25	0·6144	1·34	0·0783	1·16	0·0244	1·35	488	28	486	5	486	5	487	7
C1-36 fz		0·0564	1·15	0·5915	1·26	0·0760	1·17	0·0246	1·26	469	26	472	5	472	5	491	6
C1-43.1 fz		0·0564	1·12	0·6428	1·25	0·0827	1·19	0·0239	1·13	469	25	504	5	512	6	477	5
C1-43.2 fz	0·07	0·0582	1·84	0·6438	1·44	0·0802	1·12	0·0248	2·02	537	41	505	6	498	5	496	9
C1-46 c		0·0574	1·38	0·6390	1·47	0·0808	1·22	0·0229	1·62	506	31	502	6	501	6	457	7
C10, Howard Peaks bt-monzogranite																	
C10-1.1 tz		0·0580	1·02	0·5323	0·92	0·0666	0·92	0·0193	0·98	531	23	433	3	416	4	387	4
C10-1.2 tz		0·0679	1·03	0·7412	0·96	0·0793	0·88	0·0117	0·85	866	22	563	4	492	4	235	2
C10-5.1 c		0·0599	1·10	0·6597	1·00	0·0800	0·90	0·0242	0·91	599	24	514	4	496	4	482	4
C10-5.2 c		0·0616	1·09	0·6793	0·97	0·0801	0·89	0·0245	0·98	659	24	526	4	497	4	489	5
C10-7 c		0·0568	1·13	0·6199	1·04	0·0793	0·92	0·0233	0·90	483	25	490	4	492	4	465	4
C10-11 fz		0·0582	1·08	0·6324	0·99	0·0789	0·93	0·0247	1·01	537	24	498	4	489	4	493	5
C10-17 c		0·0592	1·08	0·6609	0·98	0·0812	0·86	0·0250	1·20	573	24	515	4	503	4	499	6
C10-60 c		0·0575	1·46	0·5930	1·43	0·0748	1·08	0·0227	1·19	511	33	473	5	465	5	453	5
C10-66.1 fz	0·20	0·0587	3·92	0·6381	3·70	0·0789	1·27	0·0243	3·29	555	88	501	15	489	6	485	16
C10-66.2 fz		0·0592	4·00	0·6377	4·09	0·0781	1·86			572	87	501	16	485	9		
M14, Howard Peaks bt-monzogranite																	
M14-10 tz		0·0585	2·03	0·5694	1·94	0·0706	1·18	0·0216	2·03	549	45	458	7	440	5	433	9
M14-12.1 c	0·23	0·0554	1·82	0·5342	1·48	0·0699	1·14	0·0217	2·76	429	42	435	5	436	5	434	11
M14-12.2 c		0·0581	2·43	0·6758	2·56	0·0844	1·46			532	54	524	10	522	7		
M14-14 fz		0·0588	3·22	0·6756	2·99	0·0833	1·08			558	70	524	12	516	5		
M14-28.1 c	2·00	0·0544	5·06	0·6203	4·85	0·0827	1·45	0·0247	4·05	387	117	490	19	512	7	493	20
M14-28.2 fz		0·0577	3·63	0·6250	3·55	0·0785	1·66			518	80	493	14	487	8		
M14-28.3 fz	0·48	0·0574	1·71	0·6141	1·40	0·0776	1·03	0·0238	2·10	506	38	486	5	482	5	476	9
M14-38 tz	0·66	0·0580	2·66	0·6102	2·44	0·0763	1·05	0·0233	2·15	529	59	484	9	474	5	466	9
DF6, Howard Peaks opx-bearing monzogranite																	
DF6-122 tz		0·0567	0·99	0·6064	0·82	0·0776	0·84	0·0247	0·85	480	22	481	3	482	4	492	4
DF6-127.1 c		0·0597	1·44	0·6169	1·35	0·0750	1·00	0·0250	1·24	591	32	488	5	466	4	499	6
DF6-127.2 c		0·0596	2·59	0·6298	2·90	0·0765	1·13			590	112	496	23	475	10		
DF6-140.1 fz	0·13	0·0565	2·35	0·5849	2·10	0·0751	1·07	0·0233	2·15	471	53	468	8	467	5	465	11
DF6-140.2 fz		0·0552	1·65	0·5689	1·73	0·0747	1·02			420	74	457	13	464	9		
DF6-146.1 c		0·0565	1·19	0·5913	1·15	0·0758	1·00	0·0237	1·44	474	27	472	4	471	5	473	7
DF6-146.2 c	0·04	0·0571	1·47	0·6080	1·07	0·0772	1·04	0·0240	2·08	496	33	482	4	479	5	479	9
DF6-146.3 c		0·0570	1·89	0·6014	1·73	0·0765	0·86			490	82	478	13	475	8		
DF6-158 fz		0·0561	4·04	0·5756	3·87	0·0743	1·70	0·0242	4·25	457	92	462	14	462	8	484	20
DF6-168.1 fz		0·0571	1·38	0·6266	1·35	0·0795	1·08	0·0228	1·18	496	31	494	5	493	5	456	5
DF6-168.2 fz		0·0570	1·58	0·5882	1·68	0·0748	0·98			490	70	470	13	465	9		
C4, Howard Peaks bt-granodiorite																	
C4-54 fz		0·0566	1·33	0·5852	1·26	0·0750	1·00	0·0228	1·23	476	30	468	5	466	4	455	6
C4-58 tz		0·0578	1·04	0·5696	0·95	0·0716	0·92	0·0219	1·00	520	23	458	3	446	4	438	4

(continued)

Table 1: Continued

Sample	f_{206} (%)	Isotopic ratios								Ages							
		^{207}Pb/ ^{206}Pb	RSD	^{207}Pb/ ^{235}U	RSD	^{206}Pb/ ^{238}U	RSD	^{208}Pb/ ^{232}Th	RSD	^{207}Pb/ ^{206}Pb	1σ	^{207}Pb/ ^{235}U	1σ	^{206}Pb/ ^{238}U	1σ	^{208}Pb/ ^{232}Th	1σ
C4-61 fz	1·15	0·0573	1·90	0·5688	1·60	0·0721	1·11	0·0218	2·75	501	43	457	6	449	5	436	11
C4-69.1 fz		0·0579	1·17	0·6355	1·06	0·0795	0·91	0·0272	1·18	527	26	499	4	493	4	542	6
C4-69.2 fz	0·15	0·0562	1·53	0·5870	1·19	0·0758	0·92	0·0235	1·70	459	35	469	5	471	4	470	9
C4-72 tz	0·46	0·0571	2·19	0·5805	1·88	0·0738	1·08	0·0227	3·52	494	49	465	7	459	5	453	16
C4-78 fz		0·0575	1·43	0·6403	1·40	0·0808	1·08	0·0254	1·38	512	32	503	6	501	5	506	7
C4-81 c		0·0589	1·56	0·6593	1·56	0·0812	1·17	0·0255	1·88	563	35	514	6	503	6	509	9
L1, bt-monzogranite from the Keinath Pluton																	
L1-46 tz	0·30	0·0549	2·06	0·4093	1·73	0·0540	1·11	0·0168	1·79	409	47	348	5	339	4	336	5
L1-47 tz		0·0570	1·09	0·6178	1·07	0·0789	1·00	0·0224	0·85	490	25	488	4	489	5	448	4
L1-49 tz		0·0569	1·09	0·6189	1·20	0·0788	1·14	0·0212	0·94	489	25	489	5	489	5	424	4
L1-53 fz		0·0567	1·09	0·6003	1·19	0·0768	1·13	0·0219	1·00	479	25	477	5	477	5	438	4
L1-57.1 fz		0·0565	1·96	0·5876	1·95	0·0754	1·21	0·0232	1·42	472	44	469	7	469	5	464	7
L1-57.2 fz		0·0565	1·22	0·5932	1·29	0·0761	1·14	0·0226	1·15	472	28	473	5	473	5	452	5
L1-69 fz		0·0570	1·39	0·6219	1·43	0·0791	1·15	0·0226	1·19	492	31	491	6	491	5	452	5
L1-75 fz		0·0570	1·23	0·6155	1·25	0·0784	1·08	0·0235	1·11	493	28	487	5	486	5	470	5
L1-86 sfz		0·0561	1·50	0·5638	1·57	0·0729	1·25	0·0187	1·34	456	34	454	6	453	5	375	5
MS1, hbl–bt-tonalite from the 'Corner Tonalite' unit																	
MS1-4 bz	6·75	0·0576	4·86	0·6584	4·72	0·0829	1·21	0·0181	3·31	514	110	514	19	514	6	362	12
MS1-7		0·0596	3·44	0·6070	3·29	0·0739	1·47	0·0252	3·02	589	76	482	13	460	7	502	15
MS1-9 bz		0·0576	1·67	0·5934	1·59	0·0748	1·07	0·0256	1·53	513	37	473	6	465	5	510	8
MS1-12	0·38	0·0552	4·71	0·5597	4·48	0·0735	1·36	0·0227	4·85	421	108	451	16	457	6	454	22
MS1-13	1·03	0·0529	4·93	0·6137	4·74	0·0841	1·31	0·0258	3·49	326	115	486	18	521	7	514	18
MS1-15.1		0·0572	1·57	0·6420	1·51	0·0813	1·06	0·0249	1·44	501	35	504	6	504	5	498	7
MS1-15.2		0·0563	2·70	0·6378	2·60	0·0822	1·34	0·0262	2·97	463	61	501	10	509	7	524	15
MS1-16		0·0567	1·55	0·5990	1·49	0·0766	1·06	0·0240	1·33	479	35	477	6	476	5	480	6
MS1-24		0·0581	4·13	0·6693	3·96	0·0836	1·72	0·0239	4·15	535	93	520	16	517	9	477	20
MS1-39	4·80	0·0570	14·78	0·6211	14·49	0·0791	2·78	0·0188	13·83	491	333	491	56	491	13	377	52
B2, hbl–bt–quartz diorite from the 'Corner Tonalite' unit																	
B2-1		0·0571	1·56	0·6275	1·58	0·0797	1·15	0·0237	1·31	497	35	495	6	494	5	473	6
B2-5		0·0573	1·52	0·6466	1·57	0·0819	1·20	0·0246	1·34	502	34	506	6	507	6	491	7
B2-7		0·0573	1·48	0·6466	1·59	0·0818	1·25	0·0233	1·33	503	33	506	6	507	6	466	6
B2-9		0·0573	1·27	0·6365	1·42	0·0806	1·25	0·0216	1·16	502	29	500	6	499	6	433	5
B2-11		0·0569	1·58	0·6165	1·66	0·0787	1·27	0·0231	1·52	486	36	488	6	488	6	462	7
B2-12		0·0566	1·34	0·5972	1·49	0·0766	1·28	0·0205	1·22	476	30	475	6	476	6	410	5
DR12, micro-monzodiorite from the mafic dyke swarm																	
DR12-93		0·0571	2·01	0·6336	2·00	0·0805	1·28	0·0196	1·43	495	45	498	8	499	6	392	6
DR12-95		0·0569	1·83	0·6168	1·85	0·0786	1·26	0·0208	1·34	487	41	488	7	488	6	416	6
DR12-103		0·0565	1·20	0·6104	1·26	0·0783	1·12	0·0231	0·95	473	27	484	5	486	5	461	4
DR12-109		0·0571	1·40	0·6214	1·45	0·0790	1·16	0·0224	1·07	493	32	491	6	490	5	449	5
DR12-114		0·0567	2·89	0·6001	2·78	0·0769	1·37	0·0221	2·17	478	66	477	11	477	6	443	9
DR12-120		0·0572	1·15	0·6323	1·22	0·0802	1·11	0·0233	0·90	498	26	498	5	497	5	465	4

The complete dataset is provided as Electronic Appendix 1. Sample names are followed by the grain number and by the analysis number (when more than one). Analysis codes indicate zircon textures as revealed by BSE/CL imaging: fz, fine-scale zoned domains; c, complex domains (unzoned, convoluted, patchy); tz, thick zoned; bz, bright zones; sfz, small faintly zoned grain. Analyses without a code denoting the textural class appear homogeneous in BSE/CL imaging. f_{206} (%) is the percentage of common ^{206}Pb, calculated by the algorithm of Andersen (2002) assuming recent lead loss.

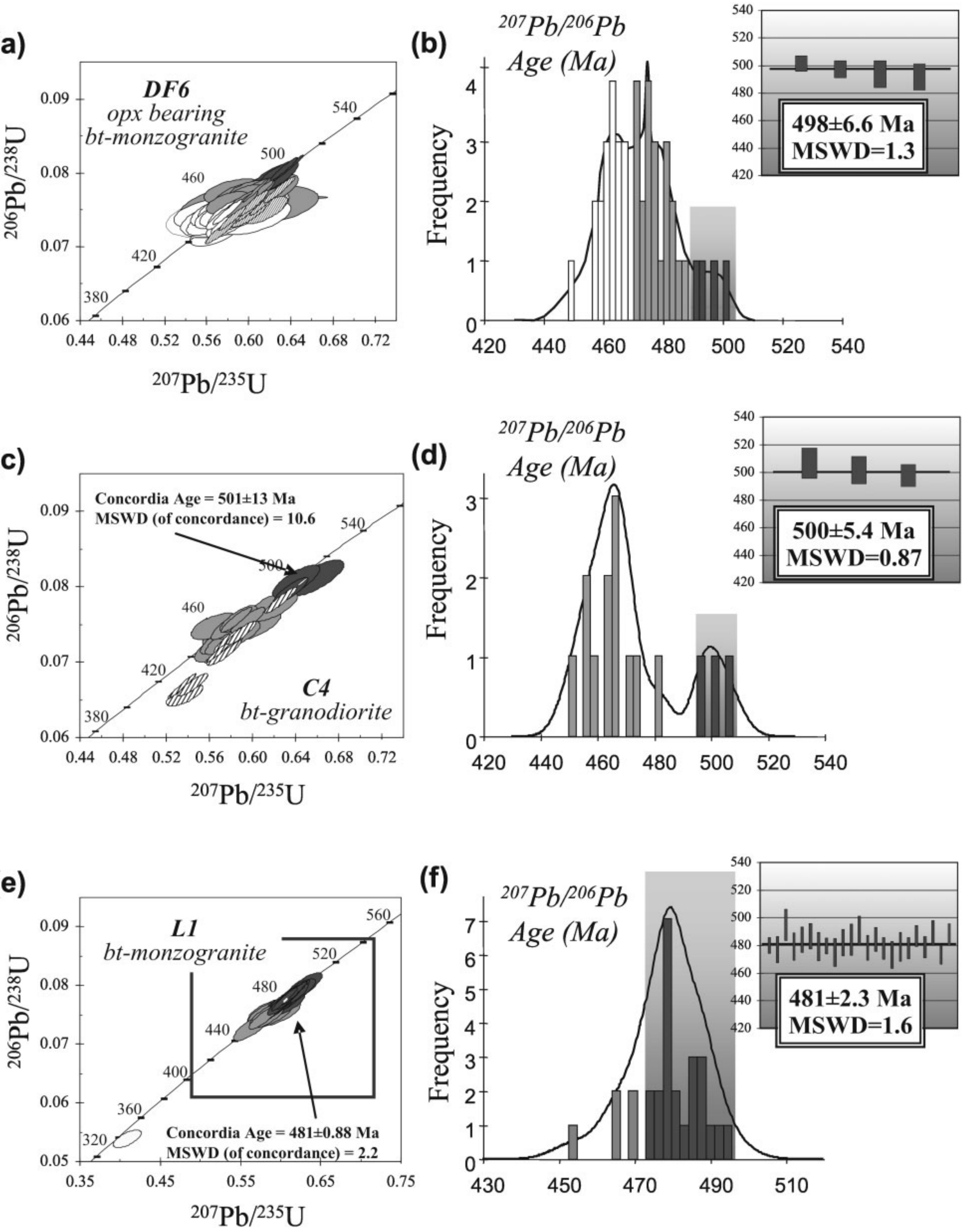

Fig. 5. Concordia (a), (c), (e), and probability density plots and weighted average ages (b), (d), (f) of LA-ICPMS U–Pb data for zircons from the Howard Peaks opx-bearing monzogranite (DF6), biotite granodiorite (C4) and Keinath biotite monzogranite (L1). Error ellipses and bars as in Fig. 4.

450 Ma, but a large number of slightly discordant ages around 470–460 Ma and three younger discordant analyses suggest that a strong Pb-loss event affected this sample. In a probability density plot and a weighted average plot (Fig. 5d) the concordant ages of this group appear to fall into two distinct populations: a minor group of three analyses that may reflect the magmatic age at 500 ± 5·4 Ma (MSWD = 0·87) and a wide cluster of younger reset ages (12 analyses) ranging from 482 to 450 Ma.

Keinath Pluton

Biotite monzogranite (sample L1)

Zircons in the biotite monzogranite L1 concentrate within the main mineral phases: K-feldspar, plagioclase and mainly biotite grains. They are generally euhedral short-prismatic to strongly elongated in shape, have sharp edges and vary in size between a few tens of microns and more than 300 μm. BSE/CL images of most grains show well-developed fine-scale oscillatory growth zoning that covers the whole grain or forms outer rims around homogeneous unzoned cores (Fig. 6a and b). In some zircons the BSE/CL images show bright thick zones, usually located in the inner rim (Fig. 6c). These bright rims often exhibit cracks. Inherited components are rare and usually occur as short-prismatic fractured grains containing bright metamict cores with typically spongy textures. More rarely they form metamict cores inside long-prismatic grains characterized by oscillatory zoning.

The U–Pb data (Table 1) for the analysed zircons are given in Table 1 and Fig. 5e. They show a range of concordant ages between 495 and 464 Ma. The weighted average age (Fig. 5f) for the main group of U–Pb data (23 analyses) is 481 ± 2·3 Ma (MSWD = 1·6), interpreted as the emplacement age of the Keinath Pluton. Thick bright zones show a range of ages similar to those obtained for the fine-scale oscillatory zones, except for a single slightly discordant age around 340 Ma. Six younger ages ranging from 470 to 340 Ma reflect lead loss and are not included in the calculation of the magmatic age.

'Corner Tonalite'

Foliated hornblende–biotite quartz diorite and tonalite (samples B2 and MS1)

Zircons from the B2 quartz diorite are all textureless (Fig. 7e and f). In tonalite sample MS1 zircons are usually unzoned or faintly zoned (Fig. 7a–d). Rounded bright patches occur within some crystals and bright irregular bands are present in a few elongated zoned crystals in sample MS1. Grain shapes vary from euhedral to subhedral. Textures resembling relict cores are absent, and apatite inclusions are common in both samples. In general, textures in the diorite–tonalite zircons are much less complex than those in the granodioritic and granitic zircons (Fig. 3a–j).

As in the granitic samples, the probability density diagram for sample MS1 (Fig. 8a) shows two populations: an older group of 17 analyses with a weighted average age of 508 ± 3·1 Ma (MSWD = 0·92), and a group of younger ages (11 analyses) that ranges from 489 to 457 Ma (Fig. 8b). The differently zoned domains show the same range in U–Pb ages (Table 1). Sample B2 shows a more restricted range of ages (Fig. 8c) than MS1. The probability density plot (Fig. 8d) exhibits a single population of 25 analyses with a weighted mean age of 497 ± 2·6 Ma (MSWD = 1·18) if a younger spot related to ancient Pb loss is rejected.

Dyke swarm

Micro-monzodiorite (sample DR 12)

Zircons from sample DR12 are typically subhedral to euhedral, homogeneous to rarely zoned (oscillatory zoning), with lengths in the range 200–50 μm (Fig. 7g and h). Apatite inclusions are common. Fifteen analyses (Table 1) yield a concordant age (Fig. 8e and f) of 489 ± 3·8 Ma (MSWD = 1·7).

ZIRCON TRACE-ELEMENT CHEMISTRY

A wide range of trace-element contents, including Y, Nb, Ba, Yb, Hf, Ta, Th, U and rare earth elements (REE), has been measured on zircons that were analysed for both U–Pb and Lu–Hf in seven of the analysed samples (C10, C1, DF6, L1, MS1, B2 and DR12) to relate the trace-element concentrations to the different textural and age domains in zircons. A detailed analysis of the zircon chemistry is required to differentiate magmatic from secondary domains in zircon and to constrain the processes involved in the zircon resetting. Ablation spots, about 20 μm in diameter, were sited near the spots used for U–Pb analyses and on similar morphological domains (Figs 3, 6 and 7).

Representative trace-element compositions are shown in Table 2. (For the complete dataset refer to Electronic Appendix 2, available for downloading from http://www.petrology.oupjournals.org.) A large scatter in trace-element concentrations is found in the zircons from HPP granitoid samples C1, C10 and DF6, with variations over several orders of magnitude in light REE (LREE). There is only limited variability, however, in heavy REE (HREE) concentrations. The elemental abundances (Table 2) range over almost the same order of magnitude in the three samples. A wide variation in Y, U, Th and Hf contents is observed, with ranges between a few tens and thousands of ppm. Sample C1 shows the highest mean values of Y, Hf, ΣREE and ΣLREE, and also the highest

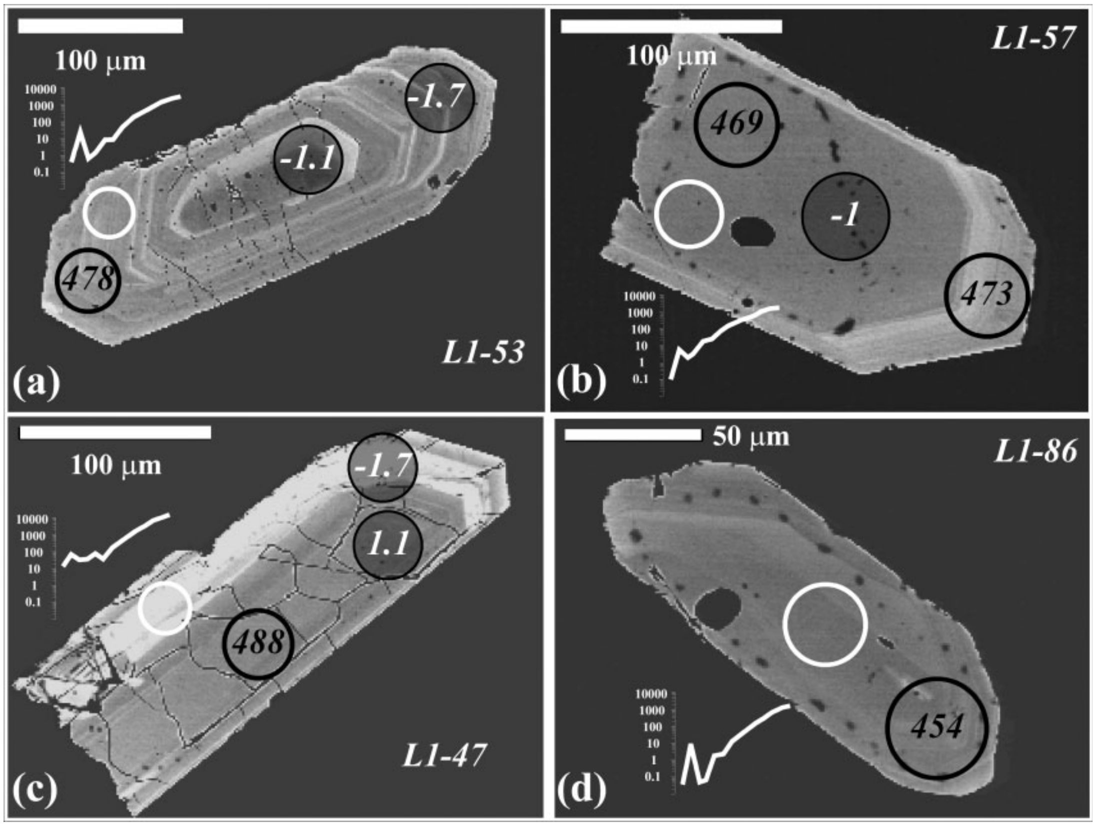

Fig. 6. BSE/CL images of representative internal textures of zircons from the Keinath Pluton biotite monzogranite (Ll). LA-ICPMS analytical sites and data as in Fig. 3. (a), (b) euhedral oscillatory zones; (c) bright thick zone intersecting the outer rim; (d) faint zoning in a small grain.

variability in LREE enrichment. A correlation can be recognized between trace-element variations and textural domains in zircons, with some differences between the three samples. In samples Cl and DF6 the domains characterized by thick zoning show the highest mean values (Table 3) for many of the measured elements. Sample Cl0 shows a different behaviour; the domains covered by fine-scale zoning have higher mean values for many elements, but again higher mean values of LREE occur in the domains with thick and complex zoning (Table 3).

The Th/U ratios range from 0·05 to 3 with a strong predominance of values higher than 0·1, typical of igneous zircons; the few low ratios (<0·1) were measured in domains with thick zoning in zircons from samples Cl0 and DF6 (Table 3). However, no clear differences can be outlined for the distinct age populations.

The REE patterns are strongly different in the three textural groups (Fig. 9a–c): the domains showing fine-scale oscillatory zoning typically have low abundances of the LREE and strongly fractionated patterns with well-defined positive Ce and negative Eu anomalies; domains characterized by thick zoning typically show enriched or flat LREE patterns with negative Eu anomalies but variable Ce anomalies; the REE abundances in the complex domains cover a wide range, overlapping with both the fine-scale and thick zoning.

The increase in the overall REE contents is related to a strong increase in the LREE contents. The LREE enrichment is always positively correlated to most of the trace elements (Y, Th, U, Yb, Nb and Ta in samples Cl and DF6). Th/U ratios are not correlated to ΣLREE in the three samples.

The zircons of the monzogranite Ll show concentrations of most of the analysed elements (U, Th, Y, Yb, Nb, Ta, Hf, REE; Tables 2 and 3) in the same range as the HPP granitoids. However, the ΣLREE in sample Ll show lower mean values and a distinctly lower variability. According to the BSE/CL images of the zircon textures (Fig. 6a–d), two of the three textural populations observed in the HPP granitoid have been recognized also in sample Ll: fine-scale zoning, which constitutes the majority of zircon grains, and thick zoning. Complex domains have not been observed. Fine-scale oscillatory zoning is characterized by LREE-depleted patterns with typical positive Ce and negative Eu anomalies (Fig. 10). The two single analyses of domains with thick zoning show LREE enrichment and higher mean contents of most of the elements

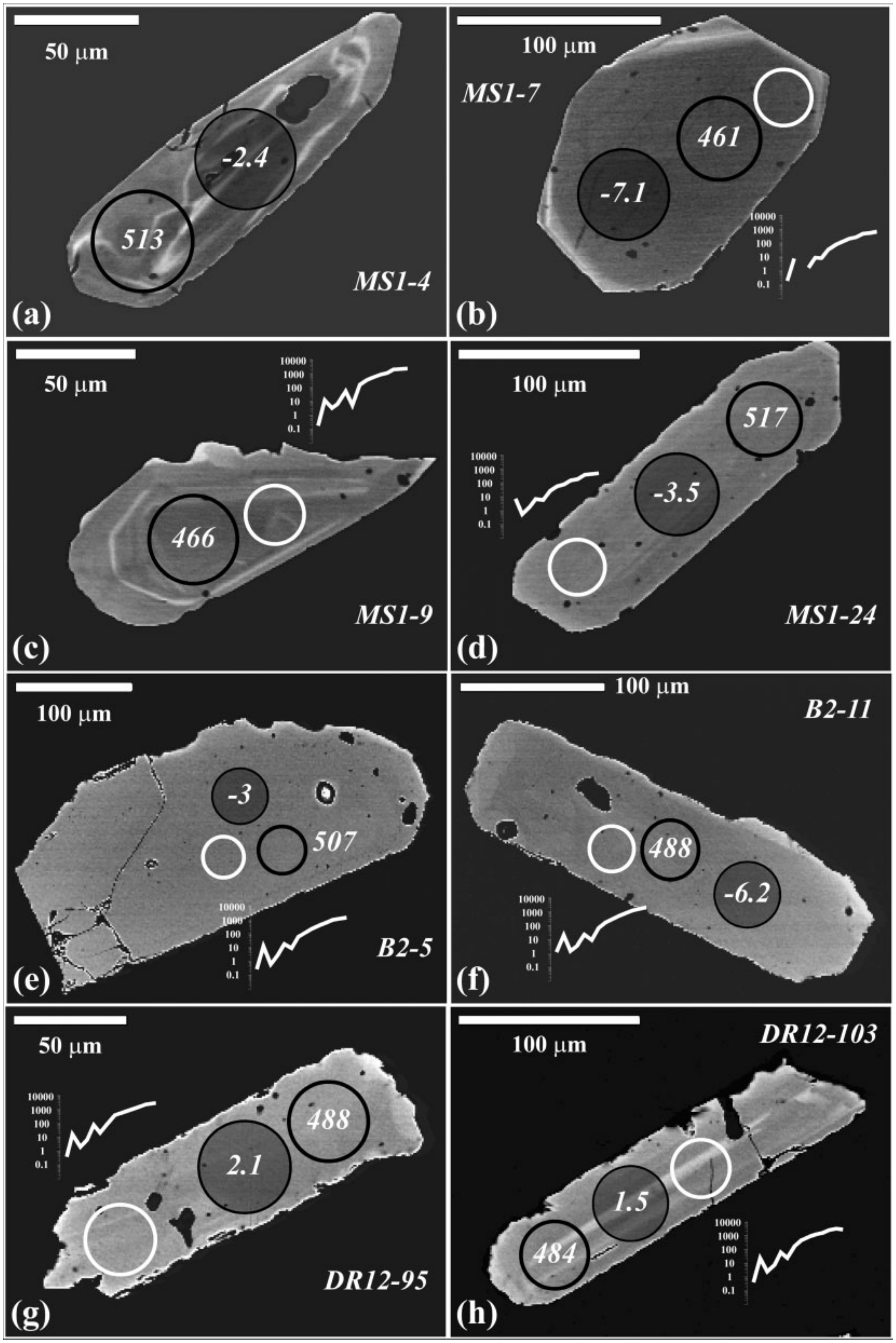

Fig. 7. BSE/CL images of representative internal textures of zircons from the tonalite (MS1) and quartz diorite (B2) samples from the 'Corner Tonalite' unit and from the micro-monzodiorite (DR12). LA-ICPMS analytical sites and data as in Fig. 3. (a), (c) bright irregular and euhedral oscillatory zones in tonalite MS1 zircons; (b), (d), (e), (f) typical texturless zircons; (g), (h) textureless and weakly planar zoned grains in the micro-monzodiorite DR12.

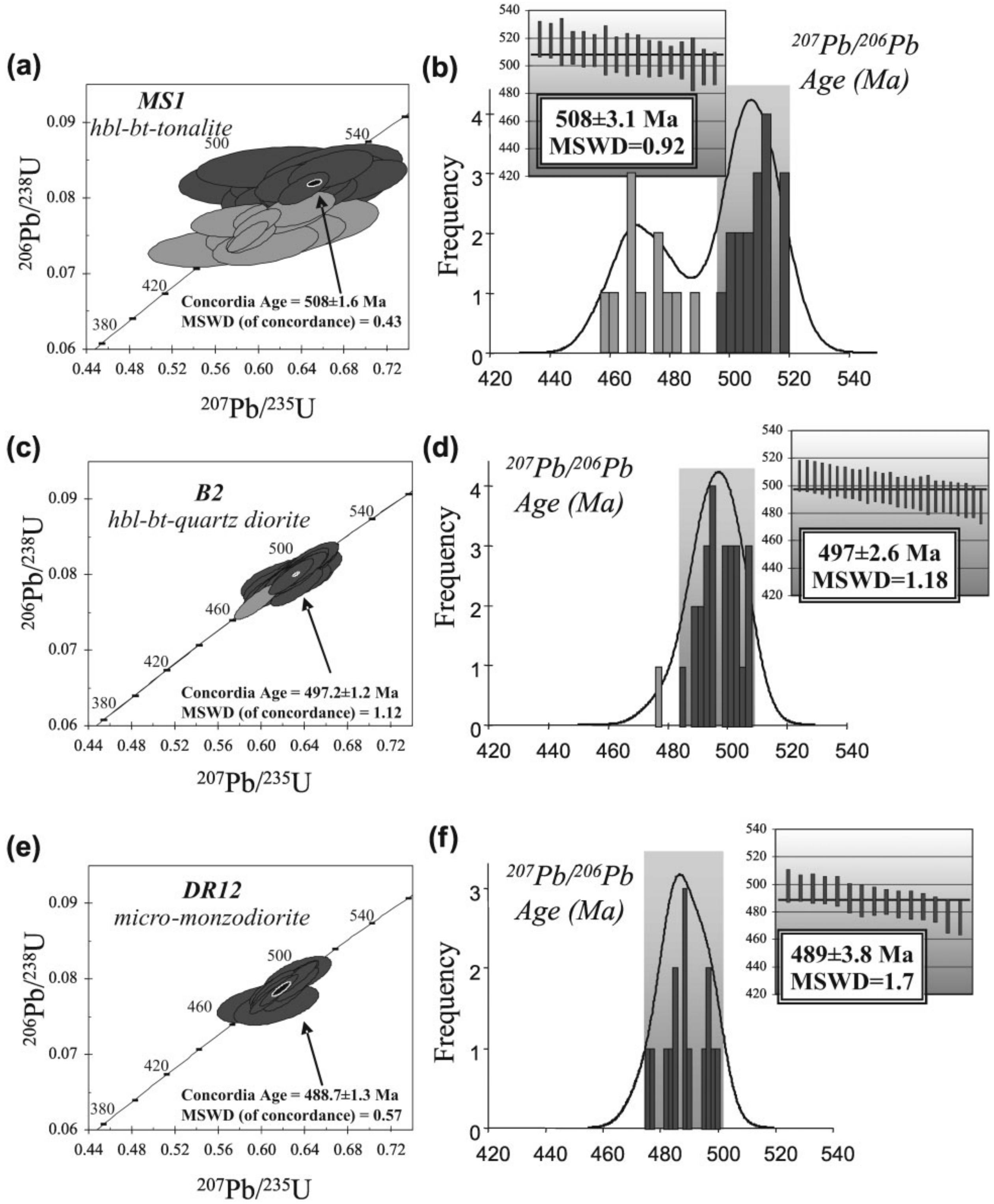

Fig. 8. Concordia (a), (c), (e), and probability density plots and weighted average ages (b), (d), (f) of LA-ICPMS U–Pb data for zircons from the tonalite (MS1) and quartz diorite (B2) samples from the 'Corner Tonalite' unit and from the micro-monzodiorite (DR12). Error ellipses and bars as in Fig. 4.

Table 2: Representative LA-ICPMS analyses of trace elements in selected zircons from six samples of the Deep Freeze Range intrusives

Sample	C1-Howard Peaks bt-monzogranite									
	C1-8	C1-9.1	C1-9.2	C1-18.1	C1-18.2	C1-43.1	C1-43.2	C1-46	C10-1.1	C10-1.2
P	742·67	466·48	547·03	1162·55	1287·39	652·70	730·93	1142·14		
Ca	203·91	564·21	291·48	494·83	1504·02	369·74	290·35	919·05	<55·25	656·53
Ti	<1·39	14·71	6·45	16·97	54·15	13·32	14·51	98·26	5·06	10·34
Sr	0·88	1·32	0·94	2·11	7·15	1·26	1·34	3·32	2·50	0·73
Y	1425·27	1910·74	1198·52	2547·25	4342·25	2188·89	2037·78	3117·60	1806·94	1341·53
Nb	4·88	5·22	3·30	5·36	9·10	4·20	4·51	7·59	5·14	4·19
Ba	0·10	0·40	<0·068	0·82	1·59	1·59	1·89	1·48	0·44	0·20
La	0·10	2·03	0·25	20·08	131·68	0·65	1·10	33·30	192·26	21·98
Ce	11·64	22·50	5·24	122·49	725·23	9·60	11·97	168·92	144·33	156·28
Pr	0·06	1·05	0·16	8·82	63·49	0·60	0·51	19·44	38·57	7·47
Nd	1·55	9·76	1·93	48·64	327·93	6·70	4·79	105·71	136·24	36·78
Sm	4·09	14·55	4·11	25·38	146·00	10·52	7·63	55·36	27·35	16·45
Eu	0·27	0·66	0·15	1·83	10·44	0·38	0·27	3·57	0·87	0·68
Gd	24·45	57·80	22·53	62·36	217·87	49·69	44·29	107·70	25·71	29·84
Tb	10·82	21·34	10·10	23·37	57·57	21·41	19·27	34·75	12·52	12·02
Dy	140·75	234·79	126·37	251·06	508·89	234·78	232·28	345·14	135·66	114·72
Ho	57·52	84·38	51·01	94·22	166·05	88·13	86·47	120·43	73·84	56·59
Er	266·76	345·87	230·54	423·96	655·41	383·25	366·48	493·71	341·77	212·16
Tm	68·22	74·21	55·93	104·30	147·57	87·21	81·79	108·49	135·17	65·89
Yb	670·34	649·88	547·12	1064·46	1419·60	847·63	795·79	1012·83	1398·24	548·43
Lu	103·48	98·58	83·71	159·63	208·26	136·81	125·18	157·12	279·60	92·07
Hf	13058·87	13652·46	13652·46	15009·22	15009·22	14161·25	14161·25	13228·47	10323·42	7167·66
Ta	2·23	1·81	1·75	3·21	4·03	3·03	3·49	4·02	5·52	2·14
Pb	12·27	30·01	7·22	16·19	32·91	19·75	15·58	27·65	8·13	9·00
Th	208·22	403·34	164·27	306·53	768·55	382·87	331·76	674·48	199·02	404·88
U	566·47	439·22	580·01	1412·95	2422·60	1002·62	851·48	1020·56	3851·25	650·82
Th/U	0·37	0·92	0·28	0·22	0·32	0·38	0·39	0·66	0·05	0·62
ΣREE	1360·04	1617·41	1139·15	2410·60	4785·99	1877·35	1777·82	2766·47	2942·13	1371·36
ΣLREE	17·44	49·89	11·69	225·41	1394·33	28·07	26·00	382·73	538·75	238·96
Textural class	fz	c/core	c/rim	tz/inner rim	tz/rim	fz/core	fz/rim	c	tz/core	tz/rim

Sample	C10, Howard Peaks bt-monzogranite					DF6, Howard Peaks opx-bearing monzogranite				
	C10-5	C10-7	C10-11	C10-60	C10-66	DF6-122.1	DF6-122.2	DF6-127	DF6-146	DF6-158
P										
Ca	1281·68	189·66	384·70	854·72	<42·75	<55·25	656·53	540·02	261·43	<42·75
Ti	50·99	5·26	2·61	7·16	16·61	5·06	10·34	15·14	4·11	16·61
Sr	0·77	0·56	0·69	0·44	0·36	2·50	0·73	3·59	0·24	0·36
Y	907·11	1041·26	1292·72	678·85	822·29	1806·94	1341·53	1713·74	1387·41	822·29
Nb	4·04	6·48	3·75	2·64	2·99	5·14	4·19	6·82	13·02	2·99
Ba	0·30	4·72	<0·183	<0·175	0·43	0·44	0·20	1·01	<0·169	0·43
La	10·73	0·91	0·10	<0·040	0·21	192·26	21·98	26·69	<0·036	0·21

(continued)

Table 2: Continued

Sample	C10, Howard Peaks bt-monzogranite					DF6, Howard Peaks opx-bearing monzogranite				
	C10-5	C10-7	C10-11	C10-60	C10-66	DF6-122.1	DF6-122.2	DF6-127	DF6-146	DF6-158
Ce	73·29	7·23	2·77	1·43	3·33	144·33	156·28	43·40	17·58	3·33
Pr	5·34	1·08	0·08	0·05	0·13	38·57	7·47	12·57	0·35	0·13
Nd	26·65	4·87	1·31	0·39	1·70	136·24	36·78	52·36	6·22	1·70
Sm	13·41	3·76	2·62	1·49	3·83	27·35	16·45	23·66	9·05	3·83
Eu	0·59	0·12	0·16	<0·030	0·26	0·87	0·68	2·63	1·30	0·26
Gd	20·68	12·53	17·03	9·67	16·03	25·71	29·84	44·85	35·63	16·03
Tb	7·83	5·88	9·00	4·48	7·50	12·52	12·02	15·42	15·13	7·50
Dy	72·53	65·52	97·48	48·45	69·04	135·66	114·72	150·28	138·03	69·04
Ho	35·16	36·48	47·49	24·95	29·73	73·84	56·59	65·34	57·61	29·73
Er	121·78	153·90	187·97	96·77	109·22	341·77	212·16	241·49	198·69	109·22
Tm	38·63	45·74	50·37	27·47	29·03	135·17	65·89	70·20	51·76	29·03
Yb	307·83	357·24	407·63	224·04	238·02	1398·24	548·43	577·57	370·18	238·02
Lu	61·61	73·48	79·28	40·80	42·71	279·60	92·07	107·91	64·43	42·71
Hf	8223·31	5985·94	6580·10	6828·59	6328·18	10323·42	7167·66	7250·63	4947·60	6328·18
Ta	2·30	2·01	1·62	1·11	0·98	5·52	2·14	2·28	2·94	0·98
Pb	9·88	77·02	8·97	4·45	5·39	8·13	9·00	19·13	8·14	5·39
Th	416·72	1319·22	143·81	68·44	75·93	199·02	404·88	189·05	113·64	75·93
U	650·00	592·34	480·72	300·76	184·64	3851·25	650·82	862·45	215·37	184·64
Th/U	0·64	2·23	0·30	0·23	0·41	0·05	0·62	0·22	0·53	0·41
ΣREE	796·06	768·73	903·29	479·99	550·74	2942·13	1371·36	1434·37	965·96	550·74
ΣLREE	129·42	17·84	6·88	3·36	9·20	538·75	238·96	158·68	33·20	9·20
Textural class	c	c	fz	c	fz	tz/inner rim	tz/rim	c	c	fz

Sample	DF6	L1 bt-monzogranite from the Keinath Pluton						MS1, hbl–bt-tonalite from the ‘Corner Tonalite’ unit		
	DF6-168	L1-47	L1-49	L1-53	L1-57	L1-75	L1-86	MS1-7	MS1-9	MS1-12
P		332·29	499·86	175·72	251·84	214·57	103·13			
Ca	133·41	<24·12	<28·96	528·78	1020·24	300·41	<15·19	<41·98	<39·70	457·72
Ti	5·31	5·76	10·23	4·23	14·18	3·80	2·16	3·36	10·53	17·80
Sr	0·23	2·37	2·57	1·11	0·47	0·67	0·68	0·52	0·82	1·21
Y	469·61	3744·03	1982·19	1135·88	902·77	1004·23	483·45	526·77	1676·89	614·61
Nb	2·52	26·85	24·40	9·94	2·24	9·88	5·06	2·87	3·81	2·98
Ba	0·25	0·24	0·93	0·31	<0·09	0·45	0·21	<0·178	<0·179	5·65
La	<0·046	4·91	4·96	0·14	0·03	0·12	0·01	0·07	0·06	0·45
Ce	4·91	70·51	52·78	21·67	5·79	20·33	8·83	6·39	10·87	7·78
Pr	<0·0194	4·12	2·78	0·09	0·19	0·03	0·01	<0·019	0·44	0·10
Nd	1·23	28·54	16·79	1·20	2·54	0·76	0·05	1·24	6·06	1·18
Sm	2·56	18·26	9·24	2·18	4·35	1·60	0·43	2·12	11·72	2·16
Eu	0·52	3·07	1·96	0·70	1·56	0·60	0·17	0·64	0·43	0·57
Gd	8·67	56·12	26·33	14·83	19·83	12·60	3·59	11·95	46·07	11·29
Tb	4·09	21·89	10·02	6·36	7·44	6·25	1·80	4·23	18·47	4·89
Dy	37·92	290·02	132·90	87·88	88·10	86·98	26·01	43·00	181·06	48·82

(continued)

Table 2: Continued

Sample	DF6	L1 bt-monzogranite from the Keinath Pluton						MS1, hbl–bt-tonalite from the ‘Corner Tonalite’ unit		
	DF6-168	L1-47	L1-49	L1-53	L1-57	L1-75	L1-86	MS1-7	MS1-9	MS1-12
Ho	16·63	142·32	57·21	37·92	32·94	37·11	12·93	17·25	73·27	22·70
Er	63·71	762·99	297·52	191·49	145·19	187·82	69·28	65·08	260·05	83·12
Tm	15·83	232·54	81·62	50·82	33·70	49·35	21·39	16·46	61·75	23·66
Yb	122·05	2455·93	918·32	555·72	332·34	563·91	258·10	125·71	456·01	188·20
Lu	24·88	521·88	196·47	104·21	59·39	113·81	54·52	24·84	80·73	37·16
Hf	5722·25	21369·06	16535·58	13567·66	8818·98	11786·90	13906·85	6251·75	6874·50	5618·87
Ta	0·45	6·94	6·33	3·68	0·57	2·58	1·88	0·44	1·61	0·52
Pb	1·12	98·02	40·86	12·36	2·46	13·00	3·25	2·20	19·69	2·57
Th	24·69	1943·75	679·64	268·13	43·47	232·26	68·74	26·98	375·29	39·52
U	57·76	3721·65	1131·05	501·12	59·39	383·62	228·15	53·36	455·01	94·64
Th/U	0·43	0·52	0·60	0·54	0·73	0·61	0·30	0·51	0·82	0·42
ΣREE	303·00	4613·10	1808·90	1075·21	733·39	1081·27	457·12	318·98	1206·99	432·09
ΣLREE	8·70	126·34	86·55	25·28	12·90	22·84	9·33	9·81	29·15	11·68
Textural class	fz	tz	tz	fz	fz	fz	sfz			

Sample	MS1, hbl–bt-tonalite from the ‘Corner Tonalite’ unit					B2, hbl–bt–quartz diorite from the ‘Corner Tonalite’ unit				
	MS1-13	MS1-15	MS1-16	MS1-24	MS1-39	B2-1	B2-5	B2-7.1	B2-7.2	B2-9
P						284·10	219·36	316·58	297·64	370·10
Ca	2634·71	<43·46	215·65	286·48	1200·63	<27·83	252·52	<37·21	848·72	<24·64
Ti	3·51	10·91	9·53	8·20	14·09	16·72	18·40	18·97	18·85	22·76
Sr	6·87	0·33	<0·126	<0·100	1·14	0·49	1·05	0·60	0·73	1·27
Y	403·92	729·84	1236·12	357·51	360·50	1222·98	867·13	1173·84	1362·84	2010·32
Nb	2·69	3·13	2·99	2·55	2·42	2·87	2·43	2·97	2·39	3·63
Ba	<0·155	0·70	<0·207	0·77	<0·147	0·25	0·64	<0·162	<0·28	0·28
La	9·39	<0·038	<0·041	<0·036	2·02	0·02	0·10	0·01	0·06	0·12
Ce	30·34	7·45	7·60	7·79	10·76	13·22	8·67	11·10	11·18	16·90
Pr	2·91	0·08	0·36	0·08	0·91	0·20	0·09	0·11	0·15	0·44
Nd	14·29	0·83	2·68	1·12	3·49	3·99	1·80	2·11	2·55	7·70
Sm	5·79	2·59	4·91	1·48	2·40	7·88	3·32	6·72	6·57	13·91
Eu	0·99	0·69	1·44	0·51	0·32	1·56	0·88	1·27	1·46	2·33
Gd	8·97	15·78	28·08	8·54	7·82	35·56	19·15	28·29	31·97	55·37
Tb	3·65	5·93	10·35	3·32	3·04	12·77	6·84	11·39	11·85	22·16
Dy	32·71	62·58	108·61	30·90	31·23	155·98	85·62	135·76	136·55	239·33
Ho	13·95	28·25	46·67	12·91	12·42	57·36	32·74	50·43	51·77	86·93
Er	50·46	104·89	163·81	44·64	45·95	232·46	150·16	221·46	212·80	348·51
Tm	13·86	27·00	41·80	12·59	12·86	49·09	33·05	46·90	45·40	71·67
Yb	103·41	229·13	315·55	100·50	106·46	421·39	279·68	402·85	391·47	612·07
Lu	19·91	44·72	58·39	17·89	18·18	72·48	51·89	72·95	71·00	106·80
Hf	6893·02	5796·20	5829·59	6469·36	6215·41	11702·10	11617·30	12465·28	12465·28	10090·95
Ta	0·44	0·67	0·48	0·44	0·38	0·65	0·61	0·65	0·68	0·61
Pb	2·46	2·91	5·46	2·78	2·60	5·11	4·59	5·89	6·59	6·34

(continued)

Table 2: Continued

Sample	MS1, hbl–bt-tonalite from the 'Corner Tonalite' unit					B2, hbl–bt–quartz diorite from the 'Corner Tonalite' unit				
	MS1-13	MS1-15	MS1-16	MS1-24	MS1-39	B2-1	B2-5	B2-7.1	B2-7.2	B2-9
Th	32·12	46·81	89·75	35·18	28·47	106·21	67·13	111·04	112·43	151·02
U	80·74	128·24	175·92	94·45	66·45	174·70	131·26	201·85	204·81	211·83
Th/U	0·40	0·37	0·51	0·37	0·43	0·61	0·51	0·55	0·55	0·71
ΣREE	310·63	529·92	790·26	242·26	257·85	1063·96	674·00	991·36	974·78	1584·25
ΣLREE	62·72	10·95	15·55	10·46	19·58	25·31	13·99	20·06	20·51	39·08
Textural class								core	rim	

Sample	B2, hbl–bt–quartz diorite from 'Corner Tonalite' unit		DR12, micro-monzodiorite from the mafic dyke swarm				
	B2-11	B2-12	DR12-93	DR12-95	DR12-103	DR12-109	DR12-120
P	360·69	357·63	356·17	259·43	371·71	471·85	479·77
Ca	1596·15	827·23	223·00	743·62	554·01	323·23	542·67
Ti	18·21	24·20	228·30	4·78	24·25	20·91	33·92
Sr	1·08	0·70	0·83	0·75	0·90	1·65	1·45
Y	1128·17	2261·98	2344·14	1763·32	1641·46	4658·27	2991·96
Nb	3·07	3·07	2·65	2·37	2·81	2·51	2·70
Ba	1·55	0·37	1·67	0·13	<0·093	0·13	0·53
La	0·43	0·08	0·20	0·14	0·16	0·17	0·32
Ce	12·64	16·06	12·95	11·83	14·14	15·35	15·86
Pr	0·22	0·46	0·58	0·34	0·39	0·67	0·70
Nd	2·35	7·28	7·71	5·41	6·53	10·15	9·38
Sm	4·95	12·30	13·36	11·90	11·77	25·03	19·71
Eu	1·03	2·52	2·46	2·07	2·19	4·35	3·84
Gd	22·94	51·73	64·47	57·51	63·43	102·68	104·69
Tb	9·17	18·27	23·77	20·56	22·65	35·09	35·76
Dy	107·88	223·14	255·90	219·08	265·44	354·67	381·23
Ho	42·18	85·38	95·80	79·19	94·26	118·64	139·94
Er	189·42	360·73	389·17	318·20	374·62	441·39	573·59
Tm	42·15	76·70	82·78	69·62	83·65	99·64	129·28
Yb	372·12	661·85	746·42	617·97	713·18	862·45	1201·34
Lu	74·42	119·06	119·09	98·44	104·54	129·41	180·25
Hf	9666·96	11532·51	11023·72	9412·56	11193·32	8140·60	12210·89
Ta	0·75	0·85	0·73	0·45	2·48	0·54	1·32
Pb	7·85	9·29	14·69	9·52	12·51	16·44	21·89
Th	148·84	193·93	286·13	235·27	306·88	362·26	451·68
U	232·18	298·16	293·81	191·91	328·74	350·70	394·39
Th/U	0·64	0·65	0·97	1·23	0·93	1·03	1·15
ΣREE	881·91	1635·56	1814·66	1512·26	1756·95	2199·69	2795·89
ΣLREE	20·60	36·18	34·80	29·62	32·99	51·37	45·97
Textural class							

The complete dataset is provided as Electronic Appendix 2. Sample numbering system and textural classes as in Table 1.

Table 3: Mean abundance values of selected elements and ratios in zircons from the different samples and in distinct textural groups within a sample (concentrations in ppm)

Sample	Y	Nb	Ba	Yb	Hf	Ta	Th	U	Th/U	ΣREE	ΣLREE
C10, bt-monzogranite											
Fine-scale zoned domains (7 analyses)											
min	822·29	2·99	0·24	238·02	6096·78	0·98	75·93	184·64	0·15	550·74	6·88
max	2880·96	7·02	30·79	1318·36	11706·48	3·18	494·07	1043·16	0·53	2724·81	29·41
mean	1592·64	4·37	8·93	565·16	7377·40	1·87	212·75	582·80	0·36	1258·54	14·18
Complex domains (8 analyses)											
min	678·85	2·64	0·30	224·04	5985·94	1·11	68·44	300·76	0·18	479·99	3·36
max	2409·47	6·82	4·72	963·48	8223·31	2·44	1319·22	1251·50	2·23	2028·28	158·68
mean	1506·76	4·94	1·92	513·87	7084·05	1·88	407·03	657·88	0·69	1190·67	54·21
Thick-zoned domains (6 analyses)											
min	1341·53	4·19	0·20	500·69	6476·46	1·48	199·02	489·69	0·05	1188·88	47·51
max	2356·71	5·62	0·74	1398·24	10323·42	5·52	1594·66	3851·25	3·07	2942·13	538·75
mean	1849·26	4·84	0·47	859·51	7978·97	2·73	656·18	1427·38	0·86	1939·76	215·29
All domains (21 analyses)											
min	678·85	2·64	0·20	224·04	5985·94	0·98	68·44	184·64	0·05	479·99	3·36
max	2880·96	7·02	30·79	1398·24	11706·48	5·52	1594·66	3851·25	3·07	2942·13	538·75
mean	1633·24	4·72	3·47	629·72	7437·53	2·12	413·45	852·71	0·63	1427·32	86·89
C1, bt-monzogranite											
Fine-scale zoned domains (10 analyses)											
min	1347·85	2·62	0·10	551·64	9327·77	1·12	134·63	382·91	0·23	1226·20	7·98
max	2818·51	5·42	1·89	943·72	14161·25	3·49	398·04	1002·62	0·56	2212·57	53·36
mean	1824·01	3·94	0·58	738·77	12965·60	2·16	250·66	696·02	0·36	1603·78	25·51
Complex domains (11 analyses)											
min	1198·52	3·06	0·12	547·12	13228·47	1·75	105·50	439·22	0·10	1139·15	11·69
max	3983·60	13·98	3·51	1363·17	17213·97	4·02	1179·17	1626·65	0·92	3488·84	386·10
mean	2339·97	6·31	1·26	990·57	14408·70	2·69	441·59	959·50	0·47	2270·19	165·51
Thick-zoned domains (5 analyses)											
min	2108·06	4·60	0·28	804·65	13822·05	1·93	209·68	665·78	0·22	1748·25	27·38
max	4342·25	9·10	1·59	1419·60	15009·22	4·03	768·55	2422·60	0·58	4785·99	1394·33
mean	2853·53	6·15	0·88	1043·31	14500·43	2·93	441·72	1350·70	0·34	2650·51	352·01
All domains (26 analyses)											
min	1198·52	2·62	0·10	547·12	9327·77	1·12	105·50	382·91	0·10	1139·15	7·98
max	4342·25	13·98	3·51	1419·60	17213·97	4·03	1179·17	2422·60	0·92	4785·99	1394·33
mean	2240·29	5·37	0·93	903·87	13871·30	2·53	368·18	933·39	0·40	2087·02	147·53
DF6, opx-bearing monzogranite											
Fine-scale zoned domains (12 analyses)											
min	469·61	2·43	0·25	122·05	5618·87	0·44	24·69	53·36	0·15	303·00	3·36
max	2880·96	5·94	5·65	1318·36	11706·48	3·04	458·22	1043·16	1·01	2724·81	30·57
mean	990·68	3·41	1·80	320·05	6622·10	0·96	104·69	237·67	0·50	733·92	12·40
Complex domains (13 analyses)											
min	357·51	2·51	0·33	100·50	4947·60	0·41	25·39	59·19	0·18	242·26	8·24
max	2409·47	13·02	4·72	1128·98	8584·64	3·86	1319·22	2151·83	2·23	2292·65	158·68
mean	1302·08	5·25	1·10	476·05	6634·19	1·93	336·81	649·79	0·62	1070·90	39·23
Thick-zoned domains (7 analyses)											
min	907·11	4·04	0·20	307·83	6476·46	1·61	199·02	489·69	0·05	796·06	43·93
max	3478·94	6·29	1·12	2040·00	10323·42	5·52	416·72	3851·25	0·64	3877·61	538·75
mean	1940·01	4·72	0·54	945·03	8106·61	3·05	310·47	1594·64	0·35	2031·89	177·71

(continued)

Table 3: Continued

Sample	Y	Nb	Ba	Yb	Hf	Ta	Th	U	Th/U	ΣREE	ΣLREE
All domains (32 analyses)											
min	357·51	2·43	0·20	100·50	4947·60	0·41	24·69	53·36	0·05	242·26	3·36
max	3478·94	13·02	5·65	2040·00	11706·48	5·52	1319·22	3851·25	2·23	3877·61	538·75
mean	1324·85	4·44	1·07	520·14	6951·75	1·81	244·00	701·93	0·52	1154·75	59·46
L1, bt-monzogranite											
Fine-scale zoned domains (13 analyses)											
min	801·60	2·24	0·09	332·34	8818·98	0·57	43·47	59·39	0·50	733·39	12·90
max	2379·37	20·80	0·46	1010·20	16535·58	6·53	501·39	777·65	0·84	2121·96	64·19
mean	1504·61	10·48	0·30	707·05	12791·43	3·66	309·14	493·50	0·64	1428·68	31·47
Thick-zoned domains (2 analyses)											
min	1982·19	24·40	0·24	918·32	16535·58	6·33	679·64	1131·05	0·52	1808·90	86·55
max	3744·03	26·85	0·93	2455·93	21369·06	6·94	1943·75	3721·65	0·60	4613·10	126·34
mean	2863·11	25·63	0·59	1687·13	18952·32	6·64	1311·70	2426·35	0·56	3211·00	106·45
Small faintly zoned grain (1 analysis)											
	483·45	5·06	0·21	258·10	13906·85	1·88	68·74	228·15	0·30	457·12	9·33
All domains (16 analyses)											
min	483·45	2·24	0·09	258·10	8818·98	0·57	43·47	59·39	0·30	457·12	9·33
max	3744·03	26·85	0·93	2455·93	21369·06	6·94	1943·75	3721·65	0·84	4613·10	126·34
mean	1610·60	12·03	0·35	801·50	13631·26	3·92	419·44	718·52	0·61	1590·75	39·46
MS1, hbl–bt-tonalite											
Structureless and faintly zoned domains (17 analyses)											
min	357·51	2·24	0·23	100·50	5260·14	0·38	25·16	53·36	0·21	242·26	5·17
max	1676·89	3·93	5·65	456·01	7949·74	1·61	375·29	455·01	0·82	1206·99	62·72
mean	678·11	2·88	1·64	194·73	6287·59	0·61	61·62	130·91	0·44	471·29	15·39
Bright zones (2 analyses)											
min	469·61	2·52	0·25	122·05	5722·25	0·45	24·69	57·76	0·27	303·00	6·15
max	1243·45	3·63	0·42	436·69	7360·78	1·43	161·00	597·73	0·43	934·35	8·70
mean	856·53	3·08	0·34	279·37	6541·52	0·94	92·85	327·75	0·35	618·67	7·42
All domains (19 analyses)											
min	357·51	2·24	0·23	100·50	5260·14	0·38	24·69	53·36	0·21	242·26	5·17
max	1676·89	3·93	5·65	456·01	7949·74	1·61	375·29	597·73	0·82	1206·99	62·72
mean	696·89	2·90	1·35	203·64	6314·32	0·64	64·91	151·63	0·43	486·80	14·55
B2, hbl–bt–quartz diorite											
(11 analyses)											
min	867·13	2·39	0·25	279·68	9666·96	0·59	67·13	131·26	0·51	674·00	13·99
max	2261·98	3·63	1·55	661·85	12465·28	0·85	193·93	298·16	0·71	1635·56	39·08
mean	1378·30	2·89	0·62	424·02	11131·65	0·69	118·07	192·14	0·61	1060·82	24·25
DR12, micro-monzodiorite											
(9 analyses)											
min	1641·46	2·00	0·13	617·97	8140·60	0·45	206·39	191·91	0·90	1512·26	29·62
max	4658·27	3·63	1·67	1295·58	12210·89	2·48	558·19	526·36	1·23	3503·45	67·71
mean	2756·86	2·62	0·62	863·61	10439·56	0·91	336·88	325·00	1·04	2161·09	40·81

(U, Th, Y, Yb, Nb, Ta, Hf, LREE). One small grain, characterized by faint zoning and by a distinctly younger age, is characterized by lower contents of many elements (Y, Nb, Ba, Yb, ΣREE and ΣLREE). The Th/U ratio is in all textural groups always higher than 0·1 and between 0·3 and 0·8.

The zircons of the amphibole-bearing quartz diorite–tonalite samples (B2 and MS1) show a more restricted

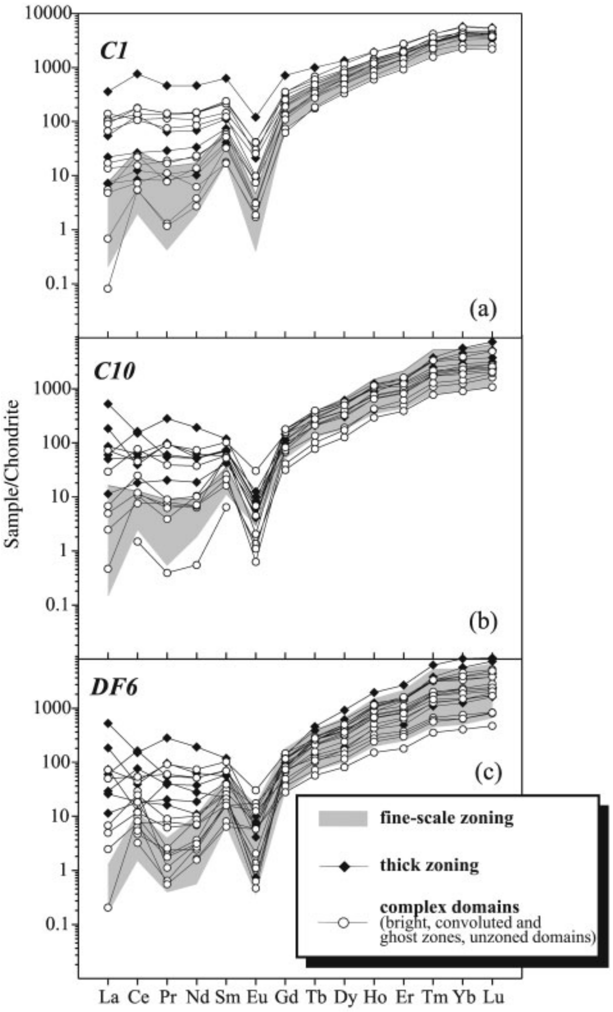

Fig. 9. (a)–(c) Chondrite-normalized REE patterns for zircons from selected samples of Howard Peaks granitoids (C1, C10 and DF6).

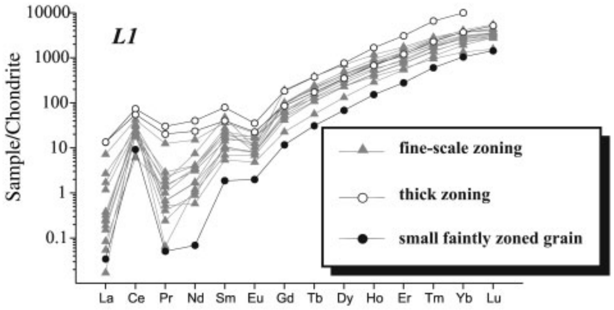

Fig. 10. Chondrite-normalized REE pattern for zircons from the biotite monzogranite (L1) from the Keinath Pluton.

variability for most of the analysed elements (U, Th, Y, Nb, Ta; Tables 2 and 3). Mean values of U, Th, Hf, Y, Yb, ΣREE and ΣLREE in sample MS1 are lower than in sample B2, and Th, U and ΣLREE show a larger variability (Table 3). The REE patterns show LREE depletion, with typical positive Ce and negative Eu anomalies (Fig. 11a and b) but are slightly less steep and more scattered in sample MS1, with larger variations in the LREE. The Th/U ratio is between 0·21 and 0·82.

The lack of visible textural domains in zircons from sample B2, and the low BSE/CL response of the MS1 zircons, hinders any attempt to relate morphological domains with microchemistry. With regard to the relationship between 'age populations' and trace-element variations, different trends are observed in the two samples: a limited LREE variability in sample B2 zircons is related to a restricted range of U–Pb ages, whereas a larger variability in ΣLREE and other measured elements and lower mean abundances in sample MS1 are connected to a larger spread in the concordant U–Pb ages.

Zircons in the micro-monzodiorite sample (DR12) have trace-element contents and REE patterns similar to those for zircons from sample B2, with slightly higher contents of U, Th, Y, Ta, ΣREE, ΣLREE and Th/U, and the same narrow range of both LREE and HREE as in sample B2 (Tables 2 and 3; Fig. 11c). In sample DR12, as observed for the quartz diorite B2 and partially for the Keinath biotite monzogranite L1, the high proportion of simple zircon textures and the limited variations of the REE are reflected in a tight clustering of the U–Pb data.

Lu–Hf ISOTOPE DATA

Zircons analysed for U–Pb were also analysed for their Hf isotopic composition. The Hf isotopic composition of zircons provides valuable information on the source and age of the protolith of the magma, and is very useful in discriminating between magmatic and inherited components. Ablation spots for the Hf analyses were sited near the spots used for U–Pb isotope analyses (Figs 3, 6 and 7). Table 4 lists the analytical data, as well as initial ϵ_{Hf} values for each grain. Lu concentrations in zircons are very low, making corrections for *in situ* decay of ^{176}Lu very small. Therefore initial ^{176}Hf/^{177}Hf values are essentially the same as measured ^{176}Hf/^{177}Hf ratios. We report the measured values in Table 4 and Fig. 12. A large number of analyses have been obtained for eight of the nine analysed samples (C10, M14, DF6, C4, MS1, B2, L1 and DR12), but here only values obtained on zircon domains with concordant ages are shown, to clearly relate zircon age and textures to Hf-isotope signature.

The spread of U–Pb ages seen in most of the analysed rocks is not reflected in the Hf isotope data. The different 'zircon age populations' observed in the granitoid and dioritic–tonalitic samples yield Hf-isotope signatures that are indistinguishable from each other, whereas significant differences are found for inherited cores (unpublished data). No correlation is evident between ^{176}Hf/^{177}Hf ratios and textural domains in zircons.

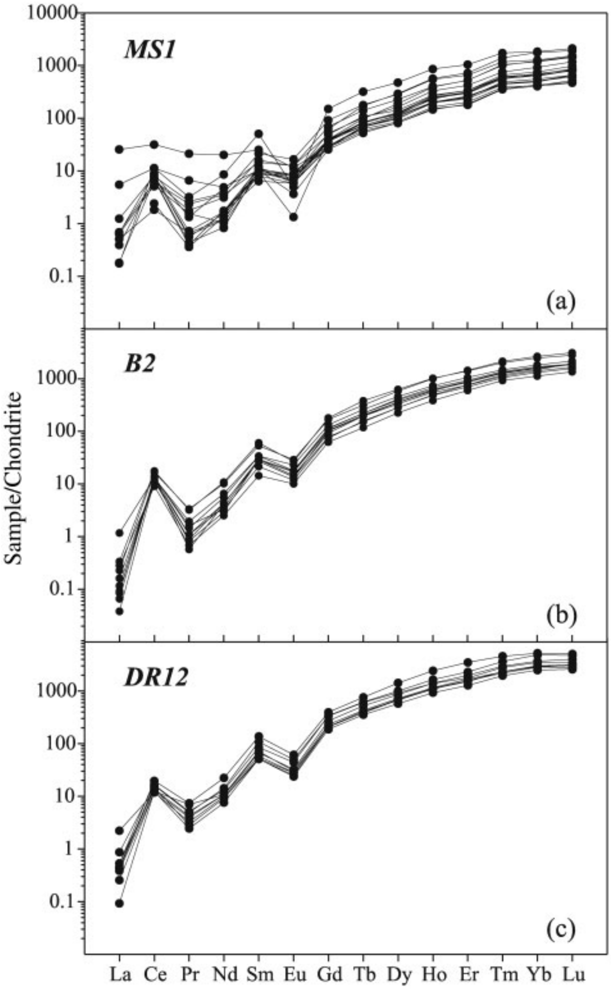

Fig. 11. Chondrite-normalized REE patterns for zircons from the tonalite (MS1) and quartz diorite (B2) samples from the 'Corner Tonalite' unit (a), (b) and from the micro-monzodiorite (DR12) (c).

The Howard Peaks granitoid and the quartz diorite and tonalite from the 'Corner Tonalite' show the same range of initial ^{176}Hf/^{177}Hf and ϵ_{Hf} (Fig. 12 and Table 4). The average ^{176}Hf/^{177}Hf is about 0·2823, and ϵ_{Hf} values are in the range between −2·1 and −10·3 in the granitoids. The T_{DM} model ages range between 1·1 and 1·5 Ga, with a mean value of 1·3 Ga. The $T_{DMcrustal}$ model age calculated for the crustal protolith (assuming ^{176}Lu/^{177}Hf = 0·015, equivalent to the average continental crust; Griffin *et al.*, 2000) ranges from 1·5 to 2·1 Ga, with a mean value of 1·8 Ga. The Corner quartz diorite and tonalite (B2 and MS1) show average ^{176}Hf/^{177}Hf ratios similar to the granitoids (0·2823) and the same range of T_{DM} and $T_{DMcrustal}$ model ages.

Zircons from the micro-monzodiorite sample DR12 have higher ^{176}Hf/^{177}Hf ratios than zircons from HPP granitoids and CT quartz diorite–tonalite samples, with values ranging from 0·2825 to 0·2824 and ε_{Hf} between −0·3 and 2·1.

The Keinath monzogranite is characterized by distinctly higher average initial ^{176}Hf/^{177}Hf relative to the HPP granitoids, around 0·2825. Such values correspond to ε_{Hf} values between −2·69 and 5·96 and a mean ε_{Hf} of 0·07. The young zircon population has ^{176}Hf/^{177}Hf ratios in the same interval. The T_{DM} model ages range between 0·87 and 1·17 Ga, with a mean value of 1·08 Ga.

DISCUSSION

The data presented here clearly indicate that in the studied granitic intrusives there is not a simple correlation between isotope data and emplacement age: the wide scatter of U–Pb data along concordia within each sample complicates the inference of the emplacement age and requires a careful evaluation of the data to discriminate possible magmatic ages from overprinted subsolidus resetting. Such discrimination can be made only if the discussion of the U–Pb data is supported by a detailed investigation and comparison of the zircon textures, as previously outlined for the analysed samples, and their trace-element and isotopic composition.

Zircon textures

Zircons from the micro-monzodiorite dyke and the CT quartz diorite–tonalite samples display a simple pattern of textures when compared with zircons from HPP granitoid samples, ranging from unzoned and homogeneous in sample B2 to unzoned to weakly zoned in samples DR12 and MS1. The following discussion will be, therefore, mainly focused on the description of the complex textures in zircons recovered from the HPP granitoid samples.

Zircons from the Keinath L1 biotite monzogranite show a predominance of fine-scale oscillatory zoning and only minor thick bright zones, similar to the thick zoning of the HPP zircons.

LA-ICPMS isotopic ages and BSE/CL imaging allow us to evaluate the roles played by different processes in each textural population of the HPP zircons, separately.

Euhedral oscillatory zoning (fine-scale and thick zoning)

The euhedrally zoned zircons show both thick and fine-scale zoning (Fig. 3a–d). Grains showing thick zoning (Fig. 3d) are characterized by the occurrence of bright zones, related to different U and Th contents in sample DF6 and U, Y, Ta and LREE in sample C10; grains with fine-scale zoning lack very bright zones but can show different degrees of oscillatory zoning. Within grains characterized by thick zoning, radial micro-fractures running perpendicular to the bright zones or fractures concentrically developed along the boundary between the bright and dark domains can occur. Such features

Table 4: Multi-collector LA-ICPMS Lu–Hf isotopic data and calculated model ages for zircons from the Deep Freeze Range intrusives

Sample	Age (Ma)	^{176}Lu/^{177}Hf	^{176}Yb/^{177}Hf	^{176}Hf/^{177}Hf	±2 S.E.	T_{DM} (Ga)	$T_{Dmcrustal}$ (Ga)	^{176}Hf/^{177}Hf$_{initial}$	ϵ_{Hf}
C10, Howard Peaks bt-monzogranite									
C10-6	478	0·000967	0·035677	0·282321	0·000020	1·27	1·75	0·282312	−5·4
C10-7	490	0·001313	0·049141	0·282325	0·000024	1·28	1·74	0·282313	−5·1
C10-10	491	0·000989	0·038309	0·282308	0·000022	1·29	1·77	0·282299	−5·6
C10-45	497	0·001490	0·057393	0·282284	0·000046	1·34	1·83	0·282270	−6·5
C10-60	467	0·001292	0·047455	0·282424	0·000022	1·14	1·54	0·282412	−2·1
M14, Howard Peaks bt-monzogranite									
M14-2	441	0·001348	0·051502	0·282297	0·000024	1·32	1·83	0·282285	−7·2
M14-3	473	0·001138	0·041329	0·282243	0·000020	1·38	1·93	0·282233	−8·3
M14-6	461	0·001704	0·068436	0·282286	0·000012	1·34	1·85	0·282271	−7·2
M14-8	485	0·001561	0·061188	0·282259	0·000017	1·38	1·90	0·282244	−7·6
M14-10	441	0·001087	0·040829	0·282274	0·000022	1·34	1·88	0·282265	−7·9
M14-12	435	0·001202	0·046155	0·282268	0·000026	1·35	1·90	0·282258	−8·3
M14-15	403	0·001618	0·061322	0·282229	0·000016	1·42	2·01	0·282216	−10·5
M14-17	457	0·001580	0·060818	0·282288	0·000017	1·34	1·85	0·282274	−7·2
M14-21	504	0·001702	0·063957	0·282258	0·000019	1·38	1·89	0·282241	−7·3
M14-22	454	0·002173	0·089624	0·282256	0·000019	1·40	1·93	0·282237	−8·6
M14-26	482	0·001324	0·055704	0·282375	0·000015	1·21	1·64	0·282363	−3·5
M14-38	474	0·001052	0·039547	0·282345	0·000020	1·24	1·71	0·282335	−4·7
M14-44	470	0·003157	0·113979	0·282378	0·000022	1·27	1·68	0·282349	−4·3
DF6, Howard Peaks opx-bearing monzogranite									
DF6-122	480	0·001299	0·041110	0·282386	0·000052	1·19	1·62	0·282374	−3·2
DF6-123	497	0·001602	0·051850	0·282273	0·000038	1·36	1·86	0·282258	−6·9
DF6-124	501	0·001848	0·061831	0·282302	0·000054	1·33	1·80	0·282284	−5·9
DF6-126	474	0·001235	0·040201	0·282250	0·000034	1·38	1·91	0·282239	−8·1
DF6-132	464	0·001597	0·055440	0·282300	0·000032	1·32	1·82	0·282286	−6·6
DF6-135	464	0·001350	0·043303	0·282284	0·000034	1·33	1·85	0·282272	−7·1
DF6-137	485	0·000724	0·023125	0·282391	0·000066	1·17	1·59	0·282384	−2·7
DF6-138	464	0·001093	0·039067	0·282401	0·000040	1·17	1·59	0·282391	−2·9
DF6-140	467	0·001370	0·044939	0·282338	0·000040	1·26	1·73	0·282326	−5·2
DF6-141	492	0·000928	0·027990	0·282342	0·000026	1·24	1·70	0·282333	−4·3
DF6-143	461	0·000871	0·028108	0·282339	0·000044	1·24	1·72	0·282331	−5·1
DF6-144	459	0·000977	0·031736	0·282296	0·000046	1·30	1·82	0·282287	−6·7
DF6-147	461	0·001273	0·041402	0·282291	0·000050	1·32	1·83	0·282280	−6·9
DF6-148	474	0·001831	0·058245	0·282325	0·000046	1·29	1·76	0·282308	−5·6
DF6-155	480	0·000678	0·021867	0·282177	0·000062	1·45	2·06	0·282171	−10·3
DF6-158	462	0·001002	0·031124	0·282333	0·000048	1·26	1·74	0·282324	−5·3
DF6-168	494	0·001198	0·038842	0·282384	0·000040	1·19	1·61	0·282373	−2·9
DF6-184	480	0·001105	0·034557	0·282245	0·000034	1·38	1·92	0·282235	−8·1
C4, Howard Peaks bt-granodiorite									
C4-46	464	0·001640	0·071674	0·282368	0·000017	1·23	1·67	0·282353	−4·3
C4-48	467	0·001396	0·057611	0·282267	0·000019	1·36	1·88	0·282254	−7·7
C4-50	464	0·001362	0·055213	0·282300	0·000014	1·31	1·81	0·282288	−6·6
C4-54	467	0·001156	0·047610	0·282267	0·000022	1·35	1·88	0·282257	−7·6
C4-55	473	0·001027	0·041024	0·282223	0·000019	1·40	1·97	0·282214	−9·0

(continued)

Table 4: Continued

Sample	Age (Ma)	^{176}Lu/^{177}Hf	^{176}Yb/^{177}Hf	^{176}Hf/^{177}Hf	±2 S.E.	T_{DM} (Ga)	$T_{DMcrustal}$ (Ga)	^{176}Hf/^{177}Hf$_{initial}$	ϵ_{Hf}
C4-67	457	0·001457	0·059176	0·282277	0·000020	1·35	1·87	0·282264	−7·6
C4-70	467	0·001091	0·044554	0·282259	0·000022	1·36	1·90	0·282249	−7·9
C4-72	460	0·002546	0·101868	0·282285	0·000020	1·38	1·87	0·282262	−7·6
L1, bt-monzogranite from the Keinath Pluton									
L1-47.1	488	0·002513	0·075109	0·282435	0·000020	1·16	1·53	0·282435	−1·7
L1-47.2	488	0·003566	0·145899	0·282660	0·000046	0·87	1·06	0·282660	6·0
L1-48	473	0·001361	0·052153	0·282404	0·000026	1·17	1·58	0·282404	−2·7
L1-49	489	0·002350	0·087990	0·282519	0·000028	1·04	1·35	0·282519	1·4
L1-51	479	0·000589	0·020617	0·282438	0·000024	1·10	1·49	0·282438	−1·1
L1-52	487	0·001490	0·058032	0·282434	0·000032	1·13	1·51	0·282434	−1·4
L1-53	478	0·001377	0·047264	0·282430	0·000026	1·14	1·53	0·282430	−1·7
L1-56	479	0·000780	0·027086	0·282481	0·000022	1·05	1·40	0·282481	0·4
L1-57	469	0·000975	0·033908	0·282451	0·000024	1·09	1·48	0·282451	−1·0
L1-58	470	0·001730	0·071277	0·282446	0·000042	1·12	1·50	0·282446	−1·4
L1-59	478	0·000780	0·027615	0·282424	0·000038	1·13	1·53	0·282424	−1·7
L1-60	484	0·001565	0·057203	0·282517	0·000028	1·02	1·34	0·282517	1·5
L1-66	464	0·001050	0·043816	0·282411	0·000034	1·15	1·57	0·282411	−2·5
L1-69	491	0·002474	0·102636	0·282580	0·000046	0·96	1·21	0·282580	3·6
L1-70	484	0·000857	0·031852	0·282443	0·000034	1·10	1·48	0·282443	−0·9
L1-71	475	0·001566	0·052671	0·282514	0·000030	1·03	1·35	0·282514	1·2
L1-72	479	0·001282	0·050138	0·282493	0·000038	1·05	1·39	0·282493	0·6
L1-74	466	0·001069	0·036625	0·282482	0·000036	1·06	1·41	0·282482	0·0
L1-76	484	0·001402	0·054167	0·282503	0·000024	1·04	1·36	0·282503	1·0
L1-79	479	0·001282	0·045908	0·282507	0·000028	1·03	1·36	0·282507	1·1
L1-81	495	0·001321	0·044398	0·282438	0·000036	1·12	1·50	0·282438	−1·0
L1-82	477	0·001305	0·050603	0·282443	0·000028	1·12	1·50	0·282443	−1·2
MS1, hbl–bt-tonalite from the 'Corner Tonalite' unit									
MS1-2	489	0·000548	0·022876	0·282241	0·000040	1·36	1·91	0·282236	−7·8
MS1-4	513	0·002445	0·121962	0·282399	0·000048	1·21	1·60	0·282375	−2·4
MS1-5	478	0·000629	0·025369	0·282242	0·000028	1·36	1·92	0·282236	−8·1
MS1-6	483	0·000336	0·012886	0·282241	0·000022	1·36	1·91	0·282238	−7·9
MS1-7	461	0·000514	0·019999	0·282279	0·000020	1·31	1·84	0·282274	−7·1
MS1-10	469	0·000339	0·011611	0·282267	0·000042	1·32	1·86	0·282264	−7·3
MS1-11	468	0·000743	0·029396	0·282358	0·000034	1·21	1·67	0·282351	−4·2
MS1-12	457	0·000604	0·024432	0·282273	0·000050	1·32	1·86	0·282268	−7·4
MS1-16	476	0·000648	0·024297	0·282343	0·000036	1·23	1·70	0·282337	−4·6
MS1-19	511	0·001407	0·055962	0·282368	0·000052	1·22	1·64	0·282354	−3·1
MS1-24	517	0·000688	0·027464	0·282347	0·000052	1·23	1·67	0·282340	−3·5
MS1-26	504	0·000964	0·041940	0·282317	0·000026	1·28	1·75	0·282308	−5·0
MS1-27	505	0·000629	0·025087	0·282337	0·000020	1·24	1·70	0·282331	−4·1
MS1-35	518	0·000942	0·036472	0·282360	0·000030	1·22	1·65	0·282351	−3·1
MS1-42	512	0·002262	0·088392	0·282366	0·000046	1·25	1·66	0·282344	−3·5
MS1-43	469	0·001592	0·066410	0·282234	0·000022	1·41	1·96	0·282220	−8·9
B2, hbl–bt-quartz diorite from the 'Corner Tonalite' unit									
B2-1	494	0·000805	0·031461	0·282284	0·000032	1·31	1·82	0·282276	−6·3
B2-2	492	0·000801	0·033418	0·282319	0·000036	1·27	1·75	0·282311	−5·1

(continued)

Table 4: Continued

Sample	Age (Ma)	^{176}Lu/^{177}Hf	^{176}Yb/^{177}Hf	^{176}Hf/^{177}Hf	±2 S.E.	T_{DM} (Ga)	$T_{Dmcrustal}$ (Ga)	^{176}Hf/^{177}Hf$_{initial}$	ϵ_{Hf}
B2-3	498	0·000801	0·034058	0·282304	0·000030	1·29	1·77	0·282296	−5·5
B2-5	507	0·000613	0·024703	0·282368	0·000032	1·20	1·63	0·282362	−3·0
B2-6	495	0·001021	0·043318	0·282362	0·000030	1·22	1·66	0·282352	−3·6
B2-7	507	0·000677	0·026728	0·282320	0·000028	1·26	1·73	0·282313	−4·7
B2-9	500	0·001060	0·043846	0·282371	0·000022	1·21	1·63	0·282361	−3·2
B2-10.1	498	0·000942	0·039093	0·282391	0·000042	1·17	1·59	0·282382	−2·5
B2-10.2	490	0·000779	0·032446	0·282265	0·000038	1·34	1·86	0·282258	−7·0
B2-11	488	0·000486	0·018821	0·282288	0·000022	1·30	1·81	0·282283	−6·2
B2-12	476	0·000858	0·036638	0·282377	0·000026	1·19	1·63	0·282369	−3·4
B2-13	489	0·000667	0·026345	0·282325	0·000032	1·25	1·73	0·282319	−4·9
B2-14	492	0·000819	0·032640	0·282368	0·000032	1·20	1·64	0·282360	−3·4
B2-16	491	0·000921	0·034969	0·282320	0·000034	1·27	1·75	0·282311	−5·1
B2-18	503	0·000804	0·031872	0·282283	0·000028	1·32	1·82	0·282275	−6·1
B2-19	500	0·000687	0·025096	0·282250	0·000030	1·36	1·89	0·282243	−7·3
B2-22	494	0·000700	0·028247	0·282275	0·000024	1·32	1·84	0·282268	−6·6
B2-25	499	0·000965	0·039822	0·282366	0·000034	1·21	1·64	0·282357	−3·3
B2-26	495	0·000570	0·023474	0·282329	0·000024	1·25	1·72	0·282324	−4·6
B2-27	505	0·000733	0·029556	0·282286	0·000024	1·31	1·81	0·282279	−5·9
B2-29	502	0·000675	0·027521	0·282266	0·000024	1·33	1·85	0·282259	−6·7
B2-30	493	0·000560	0·023159	0·282315	0·000032	1·26	1·75	0·282310	−5·1
B2-31	506	0·000967	0·038338	0·282298	0·000024	1·30	1·79	0·282289	−5·6
B2-34	501	0·001072	0·042785	0·282298	0·000028	1·30	1·79	0·282288	−5·7
DR12, micro-monzodiorite from the mafic dyke swarm									
DR12-92	497	0·000606	0·022371	0·282449	0·000046	1·09	1·46	0·282443	−0·3
DR12-93	499	0·001498	0·058851	0·282473	0·000030	1·08	1·42	0·282459	0·3
DR12-95	488	0·001172	0·045580	0·282529	0·000038	0·99	1·30	0·282518	2·1
DR12-103	484	0·001938	0·087308	0·282521	0·000032	1·03	1·34	0·282503	1·5
DR12-104	496	0·001284	0·051999	0·282486	0·000038	1·06	1·39	0·282474	0·7
DR12-106	488	0·001522	0·066667	0·282505	0·000034	1·04	1·36	0·282491	1·2
DR12-108	485	0·000917	0·035551	0·282514	0·000038	1·01	1·33	0·282505	1·6
DR12-117	487	0·001938	0·089534	0·282537	0·000030	1·00	1·30	0·282519	2·1

Sample numbering system as in Table 1. The reported age value is the concordant ^{207}Pb/^{206}Pb age.

are typical of variously metamictized zircons (Corfu *et al.*, 2003, and references therein; Geisler *et al.*, 2003). Domains covered by thick zoning often exhibit discordant ages; domains with fine-scale oscillatory zoning commonly show more concordant ages over a wide interval.

Prismatic forms and euhedral concentric zonation commonly are interpreted as indicators of primary magmatic textures reflecting crystallization from melts (Vavra, 1990; Paterson *et al.*, 1992; Hanchar & Miller, 1993). However, in our opinion this simple interpretation of internal texture is ambiguous. Recent papers have demonstrated that apparently undamaged and euhedral crystals may represent recrystallized zircon. Different types of euhedrally zoned crystals have been recognized by Black *et al.* (1986) in zircons from metamorphic rocks, where the strength of zoning reflects differently disturbed systems, characterized by different U and/or Th contents. Strongly zoned grains are usually characterized by more discordant data and more pronounced Pb-loss events. Pidgeon *et al.* (1998) explained the thickening of the primary zones and the formation of trace-element-rich bands in zircons from Archaean granites as due to the progressive migration and reconcentration of trace elements within the zircon crystals. The redistribution of trace elements within zircon grains can provide, according to Pidgeon *et al.*, a mechanism for resetting zircon U–Pb ages independent of radiation damage of the zircon lattice, giving discordant ages. The suggested mechanism for

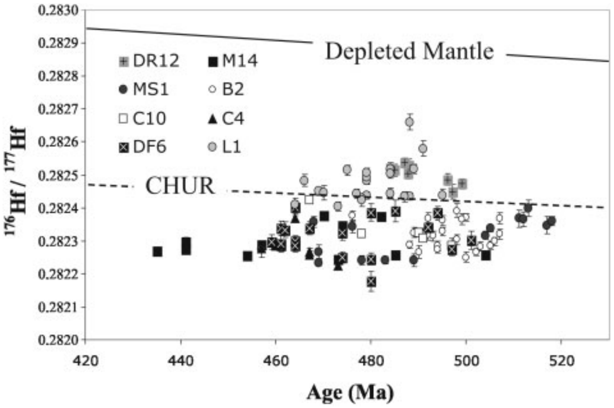

Fig. 12. ^{176}Hf/^{177}Hf in zircons from selected samples of the Deep Freeze Range intrusives, plotted against their concordant U–Pb age. Depleted Mantle and CHUR evolution lines are also shown.

producing such textures could be the instability of zoned zircon caused by the high trace-element contents, which produces a distortion of the lattice (Köppel & Sommerauer, 1974; Sommerauer, 1976). Similar conclusions were reached by Vavra *et al.* (1999) for the strongly luminescent domains related to primary structures in zircons but, in addition to thermal events, those workers attributed an important role in producing zoning-controlled alteration also to decompressional events.

A different explanation (Hartmann *et al.*, 2000) attributes paired dark–bright bands to diffusion promoted by the interaction of zircons with fluids released during metamorphic events. Such fluid-aided recrystallization could not only produce enhancement of magmatic zones by infiltration and diffusion of elements along euhedral zones, but also produce euhedral zones in originally unzoned or weakly zoned crystals.

It is clear, from this discussion, that whatever the processes that produced zircon recrystallization (solid-state or fluid-aided), euhedral zoning in crystals cannot be always interpreted as a primary texture. Dating of these crystals can sometimes yield a recrystallization age. However, most of the above-mentioned works dealt with zircons from metamorphic rocks, in which the modification of the texture was related to recrystallization under wet or dry conditions during the metamorphism. Still poorly documented is euhedral oscillatory zoning of secondary origin in magmatic rocks (unaffected by metamorphic processes). In the light of this evidence, we interpret the strongly zoned crystals in the studied granitoids as open systems in which significant Pb loss occurred, probably in a multi-stage disturbance event: an initial high-temperature solid-state recrystallization during the slow cooling of the pluton and a progressive low-temperature (probably fluid-assisted) trace-element redistribution. Large BSE/CL bright young cores could represent strongly metamict zones surrounded by outer, unaltered, euhedral rims. Bright thick zones can also, sometimes, be partially metamict, as evidenced by the presence of cracks in BSE/CL images. Zircons with fine-scale oscillatory zoning could be interpreted, on the other hand, as being as old as the strongly zoned ones, but less affected by Pb loss: the oldest ages could represent the real magmatic event, whereas the younger ones, although concordant, could be due to variable Pb loss during a single long-lasting event, which started soon after the magma emplacement.

In conclusion, constraining the magmatic age from zircons with euhedral oscillatory zoning is not always easily done, even in non-metamorphic rocks. Only crystals lacking possible evidence of secondary trace-element redistribution, such as highly luminescent bands, should be considered for discussions of the magmatic age. However, resetting phenomena also may have affected grains covered by fine-scale zoning, making a clear distinction of magmatic from reset zircons difficult on the basis of BSE/CL imaging alone.

Complex zoning

The vast majority of the studied zircons are characterized by very complex textures that show little correlation with the age results. Contorted zones (Fig. 3e–g) or (Fig. e, f and g), characterized by different BSE/CL intensity, are widespread in all the HPP granitoid samples. The curved zones usually are concentrated in the centre of the crystals (Fig. 3f, g and i), but a detailed study of the images shows that they often form protuberances starting at embayments in the crystal surfaces and invading towards the centre, leaving euhedral oscillatory zones undisturbed on the remainder of the crystal edges. Most of the investigated crystals also show BSE/CL bright domains (Fig. 3i), some of which are related to primary features in the crystal (inclusions or almost completely obliterated growth zoning), and sometimes constitute isolated patches not related to crystal terminations or inclusions in the observed two-dimensional section. A few grains also show spongy textures. Furthermore, ghosts of finely banded oscillatory zones (Fig. 3f, g, i and j) can sometimes survive between convoluted bands and spongy domains. Trace-element compositions and REE patterns in the complex domains are widely variable (Tables 2 and 3; Fig. 9a–c), with contents often intermediate or sometimes overlapping both the fine-scale and thick oscillatory zoning.

Textures similar to those described in this study have often been reported, but interpreted in different ways. The curvilinear shape of growth banding has been compared to flow structures by Vavra *et al.* (1996). In addition, the advance of contorted zones from the surface of the crystals towards the centre has been considered as evidence of resorption, and of the infiltration of hydrous fluids during metamorphism or metasomatism. Similar conclusions were reached by Pidgeon *et al.* (1998) regarding curved and contorted zoning in zircons of Archaean granites from the Darling Range Batholith. On the other hand, Hoskin & Black (2000), on the basis of the occurrence of ghost zones of magmatic oscillatory zoning within convoluted domains, argued against fluid-assisted recrystallization and favoured solid-state recrystallization. They proposed that the role of inter-granular fluids is critical only in a kinetic sense, providing higher thermal conductivity than that of the surrounding minerals. However, all of these workers agreed on the secondary origin of this kind of texture, and the discussion concerns only the mechanism responsible for the isotopic disturbance.

The wide dispersion of the U–Pb data in the samples from this study can be explained in terms of variable degrees of resetting as seen in crystals characterized by fine-scale oscillatory zoning. It is more difficult to establish the role of solid-state or fluid-assisted recrystallization. The occurrence of ghost zones between convoluted or unzoned patches and of bright domains clearly related to primary features in the crystal seem to point to a solid-state recrystallization. On the other hand, the presence of curved zones, commonly starting at the crystal edge and advancing toward the core, can be explained more easily by interaction of the crystal surface with fluids.

LREE in zircon

A number of studies (Hinton & Upton, 1991; Maas *et al.*, 1992; Barbey *et al.*, 1995; Sutherland *et al.*, 1998; Hoskin & Ireland, 2000; Hoskin *et al.*, 2000; Belousova *et al.*, 2002; Whitehouse & Kamber, 2002; Hoskin & Schaltegger, 2003) of the REE chemistry of zircon have shown that igneous zircons are characterized by steep chondrite-normalized REE patterns with a steep slope from La to Lu, and by prominent positive Ce and negative Eu anomalies. This pattern is observed for a large number of the zircons analysed in this study. However, for many of them, a scatter over three orders of magnitude in the LREE contents also has been observed, coupled with a limited variability in the HREE abundance. A xenotime-type substitution ($REE + P = Zr + Si$) has been invoked (Speer, 1982; Hinton & Upton, 1991; Hoskin *et al.*, 2000; Finch *et al.*, 2001) as the main mechanism for substitution of quadrivalent Zr by trivalent REE, the charge balance being achieved with the incorporation of P in the Si site. However, as outlined by many researchers (Speer, 1982; Hinton & Upton, 1991; Maas *et al.*, 1992; Hoskin *et al.*, 2000; Finch *et al.*, 2001; Hanchar *et al.*, 2001; Hoskin & Schaltegger, 2003), the atomic ratios of REE:P often deviate from unity, suggesting a more complex charge-balance mechanism. An excess of HREE in HREE-doped synthetic zircons has been explained by the presence of charge compensating species (Mo^{6+} and Li^{+}) in octahedral and four-coordinated interstitial sites and substitution of Zr in the Si site (Finch *et al.*, 2001; Hanchar *et al.*, 2001). However, the mechanism involved in the incorporation of large amounts of LREE is still poorly understood. The larger ionic radii of LREE cause them to be incompatible in the zircon structure and incorporated only in small amounts; the incorporation of high contents into the triangular dodecahedral site introduces a strong distortion of the zircon lattice (Whitehouse & Kamber, 2002, and references therein). Hoskin & Black (2000) proposed a mechanism of cation expulsion and recrystallization fronts progressing within the zircon lattice during subsolidus recrystallization under high-temperature conditions to explain the concentration of LREE behind the recrystallization front. In crystals subjected to similar processes, however, REE-enriched bands are usually associated with REE-depleted areas. In the analysed zircons this is true for some grains, but in many others the REE enrichment affects the whole grain. Simple volume-diffusion models can explain the mobility of HREE, but fail to explain LREE enrichments (Cherniak *et al.*, 1997), because they produce higher HREE variations with respect to LREE.

A number of workers (Bea & Montero, 1999; Schaltegger *et al.*, 1999; Rubatto, 2002; Hoskin & Schaltegger, 2003; Whitehouse & Platt, 2003) have recently related the REE patterns of zircons to the crystallization or breakdown of phases coexisting with zircon during metamorphic processes. However, although the behaviour of the HREE partitioned into zircon in equilibrium with garnet is relatively well understood, the behaviour of LREE and their relationship with LREE-rich phases such as monazite and allanite is still unknown. Fluids are important carriers of trace elements in metamorphic processes, but the mobility and immobility of REE during hydrothermal fluid–rock interaction is still a matter of debate. Rolland *et al.* (2003) described the behaviour of REE in the pre-Alpine granitic basement of Mont Blanc Massif during Alpine fluid-driven shear zone development. They suggested that the changes in REE concentrations can be mainly ascribed to the alteration of pre-existing magmatic REE-bearing minerals during deformation-related fluid–rock interaction and to the precipitation of new REE-bearing minerals. The stability of HREE- or LREE-bearing minerals is dependent on the composition of the fluids. In particular, ligands such as CO_3^{2-}, PO_4^{2-} and SO_4^{2-} and pH are important in controlling the fractionation of LREE from HREE; high sulphur fugacity values at low pH and high CO_3^{2-} contents produce LREE enrichments (Rolland *et al.*, 2003). Geisler *et al.* (2003) described strong enrichment of LREE in metamict zircons from post-tectonic granites affected by strong hydrothermal alteration related to an intensive reaction with aqueous fluids under low-temperature conditions (120–200°C).

Alternatively, as pointed out by Whitehouse & Kamber (2002), LREE enrichment of zircon can also be an analytical artefact related to the sampling of LREE-enriched phosphate inclusions not visible on the zircon surface. However, the use of time-resolved analytical techniques, as in this study, makes the recognition of such inclusions a trivial matter, if they are larger than a few microns in diameter, and none were observed in the grains described here. However, even submicroscopic inclusions of phosphate phases such as monazite or apatite should be easily detected as they are always associated with high contents of Th and Ca + Sr, respectively (Whitehouse & Kamber, 2002). A positive correlation is present in all the samples between the LREE enrichment and Th. A positive correlation is observed between ΣLREE and Ca for sample C1, but no correlation is present in samples C10 and DF6 (Table 2). This pattern could reflect, according to Whitehouse & Kamber (2002), a contamination by monazite microinclusions in samples C10 and DF6 and by monazite and/or apatite microinclusions in sample C1. However, LREE enrichment is not positively correlated with P in sample C1, which shows the best defined positive trends for both Th and Ca, except for two points (C1-13.1 and C1-20), suggesting that the above-mentioned positive correlations are, in most cases, not related to contamination by monazite and apatite microinclusions.

Lu–Hf isotope data

The relatively narrow interval of ^{176}Hf/^{177}Hf observed in zircons from the HPP granitoids and CT dioritic–tonalitic samples and the lack of correlation between ^{176}Hf/^{177}Hf ratios and textural domains in zircons exclude a restitic origin for the zircon domains characterized by relatively 'older' ages and suggest that isotopic resetting affected only the U–Pb system, leaving ^{176}Hf/^{177}Hf ratios undisturbed. Thus the Hf-isotope data strongly support the interpretation of the oldest concordant age populations in each sample as reflecting the intrusion age.

The negative ε_{Hf} values indicate the involvement of old recycled continental crust, with an age of about 1·8 Ga, in the partial melting events that generated the HPP intrusives. Low ^{176}Hf/^{177}Hf ratios and negative ε_{Hf} values (Fig. 12 and Table 4) also in the quartz diorite and tonalite samples from the 'Corner Tonalite' unit could be related to interaction processes between subduction-related mafic melts and crustal-derived components.

Within single rocks (HPP granitoids) and different age populations the Hf isotope data show small variations (Fig. 12). These ranges in the isotopic composition, which are greater than the analytical uncertainty, can be explained by two mechanisms: (1) mixing between a crustal melt and a more primitive component; (2) a heterogeneous source involved in the melting events. The large range and high values of ^{87}Sr/^{86}Sr (0·710–0·716) and low εNd (−8·9 to −7·5) of the analysed granitoids (unpublished data) are consistent with a composite crustal protolith, probably characterized by large amounts of a sedimentary component. The occurrence of a significant number of old inherited zircons in the granitoids is consistent with this model. On the other hand, the coeval mafic magmatism, which often shows magma-mingling relationships with the adjacent granitoids, could provide a more radiogenic Hf component to the crustal melts through mixing processes.

The isotopic composition of zircons from the micro-monzodiorite sample DR12, higher than that measured in zircons from HPP granitoids and CT quartz diorite and tonalite (Fig. 12), with slightly negative to positive ε_{Hf} values, is lower than that expected for zircons crystallized from a depleted mantle source, suggesting a derivation of the mafic shoshonitic rocks from an enriched mantle source, or contamination of mantle-derived melts by crustal material.

The Keinath monzogranite has slightly negative to strongly positive ε_{Hf} values. ^{176}Hf/^{177}Hf ratios extend between the CHUR and the Depleted Mantle evolution lines (Fig. 12). Such values suggest that the Keinath Pluton was derived from a source different from the Howard Peaks granitoids: probably young continental crust with an age of about 1·08 Ga which interacted with a more juvenile mantle component as suggested by the abundant mafic microgranular enclaves.

Geological implications of the isotopic data: the intrusive sequence and the tectono-magmatic evolution

The B2 sample of the 'Corner Tonalite' unit, the DR12 micro-monzodiorite dyke and the L1 monzogranite from the Keinath Pluton are all characterized by an undeformed fabric, and show narrow clusters of concordant U–Pb ages giving emplacement ages of 497 ± 2·6, 489 ± 3·8 and 481 ± 2·3 Ma, respectively. Only few analytical points (mainly in the monzogranitic sample L1) give younger ages related to Pb loss. REE patterns for the majority of analysed grains are typical of igneous zircons and the variability of all the trace elements is limited.

The geochronological data obtained on the strongly deformed Howard Peaks granitoids C1, C10, M14, DF6 and C4, and on the deformed MS1 sample from the 'Corner Tonalite' unit, show complex age spectra with a large range in the concordant data. Such complexity hinders a ready inference of the true intrusion ages from these samples. Moreover, the frequent overabundance of LREE with respect to HREE and the wide range of U, Th and Y contents exhibited by most of the studied zircons suggest that considerable mobility of these elements occurred after the crystallization of the magmatic zircons. This mobility acted in a complex way, sometimes giving rise to overabundances of LREE and large variations in Y, Th and U contents, more rarely causing the trace elements to be expelled from the zircon lattice in domains belonging to the same age population. Therefore, the best estimate of the age of intrusion cannot always be assessed from the concordant ages measured on zircons characterized by oscillatory zoning and typically magmatic trace-element patterns (steep REE patterns with negative Eu and slightly positive Ce anomalies, Th/U ratios >0·1). Indeed, the resetting of the U–Pb system is not always accompanied by the complete erasing of the magmatic textures, or by a strong modification of the typical compositional signature of the igneous zircons.

We propose that the time span over which crystallization took place can be assessed from the weighted average of the oldest (least affected by resetting of the U–Pb isotopic system) ages: the weighted average ages point to an emplacement age in the range 506–493 Ma for the Howard Peaks Pluton granitoids and of 508–497 Ma for the MS1 and B2 tonalite–quartz diorite samples. Therefore, the emplacement of the 'Corner Tonalite' intrusives appears to be coeval with the main HPP monzogranitic rocks. The intrusion of the undeformed felsic and mafic dyke swarm in the Deep Freeze Range postdates the main intrusive sequence and is documented only by the isotopic data for the single DR12 micro-monzodiorite dyke at 489 ± 3·8 Ma. Obviously more data are needed (and are in progress) to better define the emplacement age of the dyke system. The late intrusion of the undeformed Keinath Pluton is well constrained at 481 ±2·3 Ma.

These results indicate that the emplacement sequence in the Deep Freeze Range took place over a time span of at least 30 Myr, from 508 to 481 Ma, in a stress regime that varied from transpressional to extensional. The coeval intrusion of the dominant high-K megacrystic monzogranitic bodies and the high-K calc-alkaline gabbro–tonalitic ones was followed by the emplacement of the shoshonitic mafic dykes, the felsic undeformed dyke swarm and few late calc-alkaline granitic bodies. Figure 13 illustrates schematically the emplacement sequence compared with the relative volume of the intrusives inferred from field relationships and isotope data. This sequence is consistent with that obtained for the Terra Nova Intrusive Complex, Northern Victoria Land (Armienti *et al.*, 1990; Rocchi *et al.*, 2004) and for the main Cordilleran-style magmatism in the Dry Valleys region in Southern Victoria Land (Encarnación & Grunow, 1996; Cox *et al.*, 2000; Allibone & Wysoczanski, 2002). Distinctly younger ages ranging to about 435 Ma, with a large number of ages around 470 and 460 Ma, mainly in the deformed granitoids of the Deep Freeze Range, are thought to reflect minor to complete resetting of the primary zircon ages.

Isotopic data on zircons obtained in this study indicate that mainly the deformed facies underwent a strong resetting of the U–Pb isotopic system beginning soon after their emplacement, thus producing a continuous array of younger concordant ages (from emplacement ages to 435 Ma). The youngest reset U–Pb ages overlap the K–Ar ages obtained on biotite from different lithotypes (micaschists, gneisses and retrogressed granulites) sampled along a transect between the Priestley–Campbell Glaciers zone in the Deep Freeze Range (Vita *et al.*, 1991, 1994). The K–Ar data show a weighted average of 455 ± 5·8 Ma, close to the Rb/Sr ages of 453 ± 4 Ma on biotites from the same area (Armienti *et al.*, 1990, and references therein). U–Pb data on monazites, zircons and titanites from migmatites and granulitic gneisses of the same area (Klee *et al.*, 1992; Klee, 1995) give ages between 490 and 464 Ma, similar to the U–Pb ages of this study and suggesting a complex resetting of the U–Pb system also in the host metamorphic rocks, coeval with and subsequent to the emplacement of the granitoids.

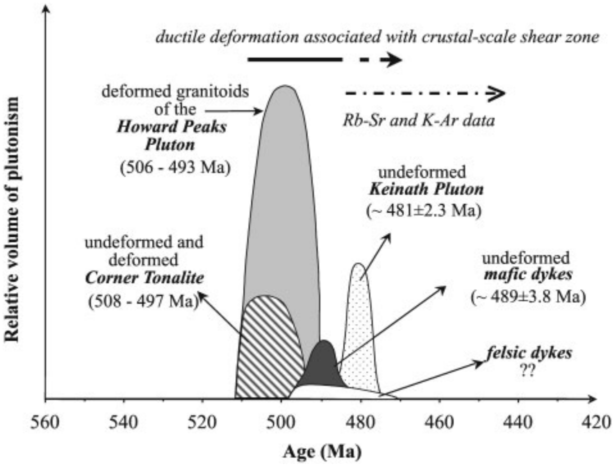

Fig. 13. Schematic plot illustrating the relative volumes and inferred emplacement age of major episodes of plutonism that occurred in the study area of the Deep Freeze Range, based on field relationships and U–Pb isotopic data. The ranges of the Rb–Sr and K–Ar data are from Tonarini & Rocchi (1994). Felsic dykes include both foliated and unfoliated dykes: no U–Pb data exist for these rocks, but an age of 484 ± 16 Ma (Rb–Sr whole-rock isochron) has been proposed for the foliated peraluminous dykes by Tonarini & Rocchi (1994).

Recent petrological and geochronological investigations on the Oates Coast metamorphic rocks (Schüssler *et al.*, 1999, 2004; Henjes-Kunst *et al.*, 2004), forming part of the western low-pressure high-temperature belt in the Wilson Terrane, as well as in the Deep Freeze Range (Grew *et al.*, 1984; Palmeri, 1991, 1997), have provided evidence for a common tectono-metamorphic evolution: a single metamorphic P–T–t loop starting at 500–490 Ma for the granulite-facies metamorphic peak down to widespread retrograde metamorphism under wet high-T conditions between 470 and 465 Ma. The post-granulite-facies metamorphic evolution as proposed by Schüssler *et al.* (1999, 2004) and Henjes-Kunst *et al.* (2004), is consistent with the data obtained in this study. However, the age of the granulite-facies metamorphic peak is still uncertain: the Howard Peaks granitoids clearly cross-cut the high-grade granulitic basement along the eastern Mt. Emison–Mt. Queensland border. We think that the 500–490 Ma age in the granulites, assumed as dating the metamorphic peak, could instead represent the age of a thermal overprint during the retrograde metamorphic evolution. The common occurrence of a sequence of intrusive mafic rocks with calc-alkaline to shoshonitic affinity in the Deep Freeze Range and in the Northern Foothills, coeval with or slightly younger (Rocchi *et al.*, 2004) than the emplacement of many granitoid bodies, is clear evidence of an important long-lasting mafic subduction-related magmatic event, responsible for the crustal melting that produced the various granitoid suites and also for the thermal input that allowed the slow cooling of the basement. The same situation is outlined in the Oates Land area, where similar mafic bodies of the Granite Harbour Intrusives are exposed (Schüssler *et al.*, 1993).

Given the above scenario, there still remains the problem of what mechanisms triggered the peculiar complex situation seen in this area: the deformation events, fluid circulation in subsolidus conditions, or a thermal input?

The abundance in the deformed intrusives of secondary trails of fluid inclusions in quartz and of fractures in the main mineral phases filled with secondary minerals (muscovite, calcite, quartz, etc.) confirms the major role played by fluids. The occurrence of an important shear system in this area and the wide distribution of minor local shear bands are probably the driving force behind the deformation and the high degree of fluid–rock interaction in the Howard Peaks intrusives. In such a setting, an extensive, fracture-assisted fluid circulation, under variable T conditions (probably sustained by the late mafic magmatism), was an important agent for the transport of Pb and trace elements from and towards the reset zircon grains. Independent fluid inclusion data for neighbouring migmatitic and granulitic rocks (Frezzotti *et al.*, 1994*a*, 1994*b*) indicate that a pervasive circulation of complex H_2O–CO_2 ($\pm CH_4$ and N_2) fluids occurred during the retrograde amphibolite-facies evolution at temperatures above 400°C, gradually evolving to a H_2O ($\pm CO_2$) dominated low-T system (Frezzotti *et al.*, 1990, and unpublished data; Giorgetti *et al.*, 1996). Data on fluid inclusions in rocks from some foliated peraluminous felsic dykes, and preliminary data from the foliated granitoids, indicate that the same types of fluid flooded these rocks. We suggest that the whole basement in the area, involved in the mega-shear zone, was affected by the same type of fluid–rock interaction process. The origin of the fluids is difficult to assess, as they could be related mainly to the mafic intrusions, as well as to a shallower source.

All the above-described basement features, documented along a linear belt extending from the Northern Foothills and Deep Freeze Range to the Matusevich Glacier area in the Oates Coast Land, are too striking to be unrelated and instead point to a common thermotectonic history of this belt. Indeed, the widespread mafic calc-alkaline to shoshonitic magmatism along this belt, clearly providing a heat source for crustal melting and production of the various granitoid suites, and the common low-P high-T evolution of the metamorphic basement in a tectonic regime evolving from transpressional to extensional, requires peculiar thermotectonic conditions. We argue that such features are consistent with models involving crustal and/or lithospheric extension in a back-arc or intra-arc environment, as proposed by several workers for the contiguous Palaeozoic Delamerian and Lachlan Fold Belts in Australia (Sandiford & Powell, 1986; Turner, 1996; Collins, 2002*a*, 2002*b*; Foden *et al.*, 2002).

CONCLUSIONS

In the Deep Freeze Range region the Cambro-Ordovician intrusive complex is constituted by a bimodal magmatic association of granitoids and mafic rocks characterized by different fabrics, that suggest a close correlation between the tectono-metamorphic events and plutonism. A ductile solid-state deformation fabric is common and overprinted on magmatic foliation in many of the intrusive bodies, suggesting a synkinematic emplacement with regional transpressional events. Some intrusions are undeformed: field relationships indicate a younger emplacement age in an extensional regime.

The U–Pb isotopic and trace-element chemistry of zircons from the major intrusive pulses of the Deep Freeze Range have been affected by a strong resetting. The probable mechanism invoked here to explain isotopic and elemental resetting is solid-state recrystallization promoted by continuous intergranular fluid circulation in an open system. Zircon characteristics and rock fabrics are interrelated: resetting is more pronounced in foliated granitoids, which were affected by late- to post-magmatic ductile deformation under subsolidus and wet conditions. The resetting process produced complex internal textures, a wide spread of concordant U–Pb ages and a strong variability of the trace-element compositions, with anomalous enrichments of LREE, U, Th and Y. Zircons in samples with undeformed fabrics exhibit, in contrast, simple internal textures, a restricted range of concordant U–Pb ages and limited variability in trace-element compositions, with REE patterns typical of magmatic undisturbed zircons. The distinct zircon age populations and different textural domains within each grain have similar Hf-isotope compositions, suggesting that the Lu–Hf system remained undisturbed.

A careful examination of the textural, isotopic and geochemical data for the zircon grains allows us to extract the emplacement age of the major intrusions in the Deep Freeze Range that covers a time span of about 30 Myr between 508 and 481 Ma. Zircon data from the undeformed intrusives indicate that the main pervasive shear deformation in this region ended at about 490 Ma.

There appear to be three main processes responsible for the observed isotopic and chemical modification of zircon: (1) extensive fluid circulation; (2) pervasive deformation; (3) protracted cooling of the whole basement. Deformation related to the occurrence of a dextral strike-slip shear zone in this area, coeval with the emplacement of the main synkinematic granitoids, provided variable degrees of fluid access. Fluid circulation probably occurred initially at high-temperature conditions, but proceeded also at low-temperature conditions. The long-lasting intrusive mafic and felsic activity provided a heat source to the whole basement, but this external heat supply alone was unable to modify zircon isotopic compositions, as clearly proven by the youngest undeformed intrusives.

The resetting process strongly affected other isotopic systems, producing a large range of K–Ar and Ar–Ar in biotites from magmatic and metamorphic rocks in the whole Deep Freeze Range (Vita *et al.*, 1991, 1994), and was probably a regional event, as suggested by a similar spread of U–Pb data in zircons from gneissic granitoid plutons in South Victoria Land (Allibone & Wysoczanski, 2002).

Our results suggest that zircon, a key mineral in modern geochronology, is not so stable as commonly assumed, particularly when water–rock interaction is involved, and the modified isotopic compositions may lead to erroneous interpretations of radiometric dating in igneous and metamorphic rocks. However, understanding the mechanisms responsible of the resetting processes is a powerful tool in unravelling metamorphic events and subsolidus phenomena in intrusive rocks.

ACKNOWLEDGEMENTS

This work was carried out with the financial support of the Italian Programma Nazionale di Ricerche in Antartide. We are grateful to Suzy Elhlou, Norm Pearson and Ashwini Sharma for their constant assistance with electron microprobe and LA-ICPMS analyses at GEMOC. We also thank Massimo Tiepolo for laboratory assistance at LA-ICPMS of CNR–Pavia. Andrew H. Allibone, Paul W. O. Hoskin, two anonymous reviewers and the editor Marjorie Wilson are gratefully acknowledged for their constructive reviews. This is Publication 445 from the ARC National Key Centre for Geochemical Evolution and Metallogeny of Continents (www.es.mq.edu.au/GEMOC/).

SUPPLEMENTARY DATA

Supplementary data for this paper are available at *Journal of Petrology* online.

REFERENCES

Adamson, R. G. (1971). Granitic rocks of the Campbell–Priestley Divide, northern Victoria Land, Antarctica. *New Zealand Journal of Geology and Geophysics* **14**, 486–503.

Allibone, A. & Wysoczanski, R. (2002). Initiation of magmatism during the Cambrian–Ordovician Ross Orogeny in southern Victoria Land, Antarctica. *Geological Society of America Bulletin* **114**, 1007–1018.

Allibone, A. H., Cox, S. C. & Smillie, R. W. (1993*a*). Granitoids of the Dry Valleys region, southern Victoria Land, Antarctica: plutons, field relations and isotopic dating. *New Zealand Journal of Geology and Geophysics* **36**, 281–297.

Allibone, A. H., Cox, S. C., Graham, I. J., Smillie, R. W., Johnstone, R. D., Ellery, S. G. & Palmer, K. (1993*b*). Granitoids of the Dry Valleys region, southern Victoria Land, Antarctica: geochemistry and evolution along the early Paleozoic Antarctic margin. *New Zealand Journal of Geology and Geophysics* **36**, 299–316.

Andersen, T. (2002). Correction of common lead in U-Pb analyses that do not report ^{204}Pb. *Chemical Geology* **192**, 59–79.

Anderson, J. L. & Smith, D. R. (1995). The effects of temperature and fO_2 in Al-in hornblende barometer. *American Mineralogist* **80**, 549–559.

Armienti, P., Ghezzo, C., Innocenti, F., Manetti, P., Rocchi, S. & Tonarini, S. (1990). Isotope geochemistry and petrology of granitoid suites from Granite Harbour intrusives of the Wilson Terrane, North Victoria Land, Antarctica. *European Journal of Mineralogy* **2**, 103–123.

Ashwal, L. D., Tucker, R. D. & Zinner, E. K. (1999). Slow cooling of deep crustal granulites and Pb-loss in zircon. *Geochimica et Cosmochimica Acta* **63**, 2839–2851.

Barbey, P., Alle, P., Brouand, M. & Albarède, F. (1995). Rare-earth patterns in zircons from the Manaslu Granite and Tibetan slab migmatites (Himalaya); insights in the origin and evolution of a crustally-derived granite magma. *Chemical Geology* **125**, 1–17.

Bea, F. & Montero, P. (1999). Behavior of accessory phases and redistribution of Zr, REE, Y, Th, and U during metamorphism and partial melting of metapelites in the lower crust; an example from the Kinzigite. *Geochimica et Cosmochimica Acta* **63**, 1133–1153.

Belousova, E. A., Griffin, W. L., Shee, S. R., Jackson, S. E. & O'Reilly, S. Y. (2001). Two age populations of zircons from the Timber Creek kimberlites, Northern Territory, as determined by laser-ablation ICP-MS analysis. *Australian Journal of Earth Sciences* **48**, 757–765.

Belousova, E. A., Griffin, W. L., O'Reilly, S. Y. & Fisher, N. I. (2002). Igneous zircon: trace element composition as an indicator of source rock type. *Contributions to Mineralogy and Petrology* **143**, 602–622.

Biagini, R., Di Vincenzo, G. & Ghezzo, C. (1991*a*). Petrology and geochemistry of peraluminous granitoids from Priestley and Aviator glacier region, Northern Victoria Land, Antarctica. *Memorie della Societa Geologica Italiana* **46**, 205–230.

Biagini, R., Di Vincenzo, G. & Ghezzo, C. (1991*b*). Mineral chemistry of metaluminous granitoids between the David and Campbell glaciers, Victoria Land, Antarctica. *Memorie della Societa Geologica Italiana* **46**, 231–247.

Black, L. P., Sheraton, J. W. & James, P. R. (1986). Late Archaean granites of the Napier Complex, Enderby Land, Antarctica;

a comparison of Rb–Sr, Sm–Nd and U–Pb isotopic systematics in a complex terrain. *Precambrian Research* **32**, 343–368.

Booth, A. L., Kolodny, Y., Chamberlain, C. P., McWilliams, M., Schmitt, A. K. & Wooden, J. (2005). Oxygen isotopic composition and U–Pb discordance in zircon. *Geochimica et Cosmochimica Act* **69**(20), 4895–4905.

Borg, S. G., Stump, E., Chappell, B. W., McCulloch, M. T., Wyborn, D., Armstrong, R. L. & Holloway, J. R. (1987). Granitoids of northern Victoria Land, Antarctica; implications of chemical and isotopic variations to regional crustal structure and tectonics. *American Journal of Science* **287**, 127–169.

Borsi, L., Ferrara, G. & Tonarini, S. (1987). Rb–Sr and K–Ar data on Granite Harbour Intrusive from Terra Nova Bay and Priestley Glacier (Victoria Land, Antarctica). *Memorie della Societa Geologica Italiana* **33**, 161–169.

Bradshaw, J. D. & Laird, M. G. (1983). The pre-Beacon geology of northern Victoria Land: a review. In: Oliver, R. L., James, P. R. & Jago, J. B. (eds) *Antarctic Earth Science*. Canberra: Australian Academy of Science, pp. 98–101.

Cherniak, D. J., Hanchar, J. M. & Watson, E. B. (1997). Rare-earth diffusion in zircon. *Chemical Geology* **134**, 289–301.

Collins, W. J. (2002*a*). Hot orogens, tectonic switching, and creation of continental crust. *Geology* **30**, 535–538.

Collins, W. J. (2002*b*). Nature of extensional accretionary orogens. *Tectonics* **21**, 6.1–6.12.

Corfu, F., Hanchar, J. M., Hoskin, P. W. O. & Kinny, P. (2003). Atlas of zircon textures. In: Hanchar, J. M. & Hoskin, P. W. O. (eds) *Zircon. Mineralogical Society of America, Reviews in Mineralogy and Geochemistry* **53**, 469–500.

Cox, S. C., Parkinson, D. L., Allibone, A. H. & Cooper, A. F. (2000). Isotopic character of Cambro-Ordovician plutonism, southern Victoria Land, Antarctica. *New Zealand Journal of Geology and Geophysics* **43**, 501–520.

Dallai, L., Ghezzo, C. & Sharp, Z. D. (2003). Oxygen isotope evidence for crustal assimilation and magma mixing in the Granite Harbour Intrusives, Northern Victoria Land, Antarctica. *Lithos* **67**, 135–151.

Di Vincenzo, G., Rocchi, S., Ghezzo, G., Andriessen, P. A. M & Ricci, C. A. (1997). Felsic and mafic magmas in the Terra Nova Intrusive Complex (Northern Victoria Land, Antartica). In: Ricci C. A. (ed.) *The Antarctic region: geological evolution and processes*. Siena: Terra Antarctica, pp. 253–263.

Di Vincenzo, G. & Rocchi, S. (1999). Origin and interaction of mafic and felsic magmas in an evolving late orogenic setting: the early Paleozoic Terra Nova Intrusive Complex, Antarctica. *Contributions to Mineralogy and Petrology* **137**, 15–35.

Encarnación, J. & Grunow, A. (1996). Changing magmatic and tectonic styles along the paleo-Pacific margin of Gondwana and the onset of early Paleozoic magmatism in Antarctica. *Tectonics* **15**, 1325–1341.

Fenn, G. (1993). Petrogenese der Granite Harbour Intrusives in Nord Victoria Land und der Prince Albert Mountains (Antarktis). Dr. thesis, University of Bremen, 174 pp.

Finch, R. J., Hanchar, J. M., Hoskin, P. W. O. & Burns, P. C. (2001). Rare-earth elements in synthetic zircon; Part 2, A single-crystal X-ray study of xenotime substitution. *American Mineralogist* **86**, 681–689.

Foden, J. D., Elburg, M. A., Turner, S. P., Sandiford, M., O'Callaghan, J. & Mitchell, S. (2002). Granite production in the Delamerian Orogen, South Australia. *Journal of the Geological Society, London* **159**, 557–575.

Frezzotti, M. L. & Talarico, F. (1990). Preliminary investigations on fluid inclusions in orthopyroxene-garnet-cordierite granulites from Boomerang Glacier (Deep Freeze Range, North Victoria Land, Antarctica): evidence of mixed CO_2–CH_4 fluids. *Memorie della Societa Geologica Italiana* **43**, 59–66.

Frezzotti, M. L., Di Vincenzo, G. & Ghezzo, C. (1994*a*). Fluid regimes in Cambro-Ordovician granitoids from Northern Victoria Land, Antarctica. *Terra Antartica* **1**, 43–45.

Frezzotti, M. L., Di Vincenzo, G., Ghezzo, C. & Burke, E. A. J. (1994*b*). Evidence of magmatic CO_2-rich fluids in peraluminous graphite-bearing leucogranites from Deep Freeze Range (northern Victoria Land, Antarctica). *Contributions to Mineralogy and Petrology* **117**, 111–123.

Gebauer, D. & Gruenenfelder, M. (1976). U–Pb zircon and Rb–Sr whole-rock dating of low-grade metasediments; example, Montagne Noire (southern France). *Contributions to Mineralogy and Petrology* **59**, 13–32.

Geisler, T., Pidgeon, R. T., Kurtz, R., van Bronswijk, W. & Schleicher, H. (2003). Experimental hydrothermal alteration of partially metamict zircon. *American Mineralogist* **88**, 1496–1513.

Ghezzo, C., Baldelli, C., Biagini, R., Carmignani, L., Di Vincenzo, G., Gosso, G., Lelli, A., Lombardo, B., Montrasio, A., Pertusati, P. C. & Salvini, F. (1987). Granitoids from the David Glacier–Aviator Glacier segment of the Transantarctic Mountains, Victoria Land, Antarctica. *Memorie della Societa Geologica Italiana* **33**, 143–159.

Giacomini, F., Bomparola, R. M. & Ghezzo, G. (2005). Petrology and geochemistry of metabasites with eclogite facies relics from NE Sardinia: constraints for the Palaeozoic evolution of Southern Europe.. *Lithos* **82**, 221–248.

Giorgetti, G., Frezzotti, M. L. E., Palmeri, R. & Burke, E. A. J. (1996). Role of fluids in migmatites; CO_2–H_2O fluid inclusions in leucosomes from the Deep Freeze Range migmatites (Terra Nova Bay, Antarctica). *Journal of Metamorphic Geology* **14**, 307–317.

Goodge, J. W. (2002). From Rodinia to Gondwana: supercontinent evolution in the Transantarctic Mountains. *Royal Society of New Zealand Bulletin* **35**, 61–74.

Goodge, J. W., Williams, I. S. & Myrow, P. (2004*a*). Provenance of Neoproterozoic and lower Paleozoic siliciclastic rocks of the central Ross orogen, Antarctica: detrital record of rift-, passive-, and active-margin sedimentation. *GSA Bulletin* **116**(9–10), 1253–1279.

Goodge, J. W., Myrow, P., Phillips, D., Fanning, C. M. & Williams, I. S. (2004*b*). Siliciclastic record of rapid denudation in response to convergent-margin orogenesis, Ross orogen, Antarctica. In: Bernet, M. & Spiegel, C. (eds) *Detrital Thermochronology—Provenance Analysis, Exhumation, and Landscape Evolution in Mountain Belts. Geological Society of America, Special Papers* **378**, 101–122.

Grew, E. S., Kleinschmidt, G. & Schubert, W. (1984). Contrasting metamorphic belts in North Victoria Land, Antarctica. *Geologisches Jahrbuch* **B60**, 253–264.

Griffin, W. L., Pearson, N. J., Belousova, E., Jackson, S. E., van Achterbergh, E., O'Reilly, S. Y. & Shee, S. R. (2000). The Hf isotope composition of cratonic mantle; LAM-MC-ICPMS analysis of zircon megacrysts in kimberlites. *Geochimica et Cosmochimica Acta* **64**, 133–147.

Gunn, B. M. & Warren, G. (1962). Geology of Victoria Land between the Mawson and Molock Glaciers, Antarctica. *New Zealand Geological Survey Bulletin* **71**, 1–157.

Hanchar, J. M. & Miller, C. F. (1993). Zircon zonation patterns as revealed by cathodoluminescence and backscattered electron images: implications for interpretation of complex crustal histories. *Chemical Geology* **110**, 1–13.

Hanchar, J. M., Finch, R. J., Hoskin, W. O., Watson, E. B., Cherniak, D. J. & Mariano, A. N. (2001). Rare earth elements in synthetic zircon; Part 1, Synthesis, and rare earth element and phosphorus doping. *American Mineralogist* **86**, 667–680.

Hartmann, L. A., Leite, J. A. D., Da Silva, L. C., Remus, M. V. D., McNaughton, N. J., Groves, D. I., Fletcher, I. R., Santos, J. O. S. & Vasconcellos, M. A. Z. (2000). Advances in SHRIMP geochronology and their impact on understanding the tectonic and metallogenic evolution of southern Brazil. *Australian Journal of Earth Sciences* **47**, 829–844.

Henjes-Kunst, F., Roland, N. W., Dunphy, J. M. & Fletcher, I. R. (2004). SHRIMP U–Pb dating of high-grade migmatites and related magmatites from northwestern Oates Land (East Antarctica): evidence for a single high-grade event of Ross-Orogenic age. *Terra Antartica* **11**(1), 67–84.

Hinton, R. W. & Upton, B. G. J. (1991). The chemistry of zircon: variations within and between large crystals from syenite and alkali basalt xenoliths. *Geochimica et Cosmochimica Acta* **55**, 3287–3302.

Hirata, T. & Nesbitt, R. W. (1995). U–Pb isotope geochronology of zircon: evaluation of the laser probe–inductively coupled plasma mass spectrometry technique. *Geochimica et Cosmochimica Acta* **59**, 2491–2500.

Hoskin, P. W. O. & Black, L. P. (2000). Metamorphic zircon formation by solid-state recrystallization of protolith igneous zircon. *Journal of Metamorphic Geology* **18**, 423–439.

Hoskin, P. W. O. & Ireland, T. R. (2000). Rare earth element chemistry of zircon and its use as a provenance indicator. *Geology* **28**, 627–630.

Hoskin, P. W. O. & Schaltegger, U. (2003). The composition of zircon and igneous and metamorphic petrogenesis. In: Hanchar, J. M. & Hoskin, P. W. O. (eds) *Zircon. Mineralogical Society of America, Reviews in Mineralogy and Geochemistry* **53**, 27–62.

Hoskin, P. W. O., Kinny, P. D., Wyborn, D. & Chappell, B. W. (2000). Identifying accessory mineral saturation during differentiation in granitoid magmas: an integrated approach. *Journal of Petrology* **41**, 1365–1396.

Jackson, S. E., Pearson, N. J., Griffin, W. L. & Belousova, E. (2004). The application of laser ablation–inductively coupled plasma–mass spectrometry (LA-ICP-MS) to *in situ* U–Pb zircon geochemistry. *Chemical Geology* **211**, 47–69.

Klee, S. (1995). Altersbestimmung hochmetamorpher Gesteine des Sudlichen Wilson-Terranes, Nord-Victora land, Antarktis. *Berichte zur Polarforschung* **60**, 50–56.

Klee, S., Baumann, A. & Thiedig, F. (1992). Age relations of the high grade metamorphic rocks in the Terra Nova Bay area, North Victoria Land, Antarctica: a preliminary report. *Polarforschung* **60**, 101–106.

Kleinschmidt, G. & Tessensohn, F. (1987). Early Paleozoic westward directed subduction at the Pacific margin of Antarctica. In: McKenzie, G. D. (ed.) *Gondwana Six: Structure, Tectonics and Geophysics*. Washington, DC: American Geophysical Union, pp. 89–105.

Kleinschmidt, G., Buggish, W. & Flottmann, T. (1992). Compressional causes for early Paleozoic Ross Orogen evidence from Victoria Land and Shackleton Range. In: Kaminuma, K. & Yoshida, Y. (eds) *Recent Progress in Antarctic Earth Science*. Tokyo: Terra, pp. 227–233.

Köppel, V. & Sommerauer, J. (1974). Trace elements and the behaviour of the U–Pb system in inherited and newly formed zircons. *Contributions to Mineralogy and Petrology* **43**, 71–82.

Kreuzer, H., Hohndorf, A., Lenz, H., Muller, P. & Vetter, U. (1987). Radiometric ages of Pre-Mesozoic rocks from Northern Victoria Land, Antarctica. In: McKenzie, G. D. (ed.) *Gondwana Six: Structure, Tectonics and Geophysics*. Washington, DC: American Geophysical Union, pp. 31–47.

Kruhl, J. H. (1996). Prism- and basal-plane parallel subgrain boudaries in quartz: a microstructural geothermobarometer. *Journal of Metamorphic Geology* **14**, 581–589.

Läufer, A. L. & Rossetti, F. (2003). Late-Ross ductile deformation features in the Wilson Terrane of northern Victoria Land (Antarctica) and their implications for the western front of the Ross Orogen. *Terra Antartica* **10**(3), 179–196.

Liermann, H. P., Isachsen, C., Altenberger, U. & Oberhänsli, R. (2002). Behavior of zircon during high-pressure, low-temperature metamorphism: case study from the Internal Unit of the Sesia Zone (Western Italian Alps). *European Journal of Mineralogy* **14**, 61–71.

Ludwig, K. R. (1999). *Isoplot/Ex 2.06, a geochronological toolkit for Microsoft Excel. Berkeley Geochronology Center Special Publications*, **1a**, 1–49.

Maas, R., Kinny, P. D., Williams, I. S., Froude, D. O. & Compston, W. (1992). The Earth's oldest known crust: a geochronological and geochemical study of 3900–4200 Ma old detrital zircons from Mt. Narryer and Jack Hills, Western Australia. *Geochimica et Cosmochimica Acta* **56**, 1281–1300.

Matzer, S. (1995). Palaozoische Akkretion am palaopazifischen Kontinentalrand der Antarktis in Nordvictorialand—*P–T–D*-Geschichte und Deformationsmechanismen im Bowers Terrane. *Berichte zur Polarforschung* **173**, 1–234.

Musumeci, G. & Pertusati, P. C. (2000). Structure of the Deep Freeze Range–Eisenhower Range of the Wilson Terrane (North Victoria Land, Antarctica); emplacement of magmatic intrusions in the early Palaeozoic deformed margin of the East Antarctic Craton. *Antarctic Science* **12**, 89–104.

Olesch, M., Roland, N. W., Fenn, G. & Krauss, U. (1996). Petrogenesis of granitoid rocks of Oates Land, Antarctica. *Geologisches Jahrbuch* **B89**, 195–245.

Palmeri, R. (1997). *P–T* paths and migmatite formation: an example from Deep Freeze Range, northern Victoria Land, Antarctica. *Lithos* **42**, 47–66.

Palmeri, R., Talarico, F., Meccheri, M., Oggiano, G., Pertusati, P. C., Rastelli, N. & Ricci, C. A. (1991). Progressive deformation and low pressure/high temperature metamorphism in the Deep Freeze Range, Wilson Terrane, northern Victoria Land, Antarctica. *Memorie della Societa Geologica Italiana* **46**, 164–179.

Passchier, C. W. & Trouw, R. A. (2005). *Microtectonics*. Berlin: Springer, 366 pp.

Paterson, S. R., Vernon, R. H. & Tobisch, O. T. (1989). A review of criteria for the identification of magmatic and tectonic foliations in granitoids. *Journal of Structural Geology* **11**, 349–363.

Paterson, B. A., Stephens, W. E., Rogers, G., Williams, I. S., Hinton, R. W. & Herd, D. A. (1992). The nature of zircon inheritance in two granite plutons. *Transactions of the Royal Society of Edinburgh: Earth Sciences*, **83**, 459–471.

Pidgeon, R. T. (1992). Recrystallization of oscillatory zoned zircon: some geochronological and petrological implications. *Contributions to Mineralogy and Petrology* **110**, 463–472.

Pidgeon, R. T., Nemchin, A. A. & Hitchen, G. J. (1998). Internal structures of zircons from Archaean granites from the Darling Range Batholith: implications for zircon stability and the interpretation of zircon U–Pb ages. *Contributions to Mineralogy and Petrology* **132**, 288–299.

Rocchi, S., Di Vincenzo, G. & Ghezzo, C. (2004). The Terra Nova Intrusive Complex (Victoria Land, Antarctica). *Terra Antartica Reports* **10**, 1–49.

Roland, N. W., Läufer, A. L. & Rossetti, F. (2004). Revision of the terrane model of northern Victoria Land (Antarctica). *Terra Antartica* **11** (1), 55–65.

Rolland, Y., Cox, S., Boullier, A. M., Pennacchioni, G. & Mancktelow, N. (2003). Rare earth and trace element mobility in mid-crustal shear zones: insights from the Mont Blanc Massif (Western Alps). *Earth and Planetary Science Letters* **214**, 203–219.

Rubatto, D. (2002). Zircon trace element geochemistry; partitioning with garnet and the link between U–Pb ages and metamorphism. *Chemical Geology* **184**, 123–138.

Rubatto, D. & Hermann, J. (2002). Zircon formation during fluid circulation in eclogites (Monviso, Western Alps): implications for Zr and Hf budget in subduction zones. *Geochimica et Cosmochimica Acta* **67**, 2173–2187.

Rubatto, D., Gebauer, D. & Compagnoni, R. (1999). Dating of eclogite-facies zircons: the age of Alpine metamorphism in the Sesia–Lanzo Zone (Western Alps). *Earth and Planetary Science Letters* **167**, 141–158.

Rubatto, D., Williams, I. S. & Buick, I. S. (2001). Zircon and monazite response to prograde metamorphism in the Reynolds Range, central Australia. *Contributions to Mineralogy and Petrology* **140**, 458–468.

Salvini, F., Brancolini, G., Busetti, M., Storti, F., Mazzarini, F. & Coren, F. (1997). Cenozoic geodynamics of the Ross Sea Region, Antarctica. Crustal extension, intraplate strike-slip faulting and tectonic inheritance. *Journal of Geophysical Research* **102**, 24669–24696.

Sandiford, M. & Powell, R. (1986). Deep crustal metamorphism during continental extension: modern and ancient examples. *Earth and Planetary Science Letters* **79**, 151–158.

Schaltegger, U., Fanning, C. M., Maurin, J. C., Schulmann, K. & Gebauer, D. (1999). Growth, annealing and recrystallization of zircon and preservation of monazite in high-grade metamorphism: conventional and *in situ* U–Pb isotope, cathodoluminescence and microchemical evidence. *Contributions to Mineralogy and Petrology* **134**, 186–201.

Schüssler, U., Skinner, D. N. B. & Roland, N. W. (1993). Subduction-related mafic to intermediate plutonism in the northwestern Wilson Terrane, North Victoria Land and Oates Coast, Antarctica. *Geologisches Jahrbuch* **E47**, 389–417.

Schüssler, U., Bröcker, M., Henjes-Kunst, F. & Will, T. (1999). P–T–t evolution of the Wilson Terrane metamorphic basement at the Oates Coast, Antarctica. *Precambrian Research* **93**, 235–258.

Schüssler, U., Henjes-Kunst, F., Talarico, F. & Flöttman, T. (2004). High-grade crystalline basement of the northwestern Wilson Terrane at Oates Coast: new petrological and geochronological data and implications for its tectonometamorphic evolution. *Terra Antartica* **11** (1), 15–34.

Skinner, D. N. B. (1991). Metamorphic basement contact relations in the southern Wilson Terrane, Terra Nova Bay, Antarctica—the Boomeraqng thrust. *Memorie della Società Geological Italiana* **46**, 163–178.

Sommerauer, J. (1976). Die Chemisch–Physikalische Stabilität Natürlicher Zirkone und ihr U–(Th)–Pb System. Dr. thesis, ETH Zürich.

Speer, J. A. (1982). Zircon. In: Ribbe, P. H. (ed.) *Orthosilicates. Mineralogical Society of America, Reviews in Mineralogy* **5**, 67–112.

Storti, F., Rossetti, F., Läufer, A. L. & Salvini, F. (2006). Consistent kinematic architecture in the damage zones of intraplate strike-slip fault systems in North Victoria Land, Antarctica and implications for fault zone evolution. *Journal of Structural Geology* **28**, 50–63.

Stump, E. (1995). *The Ross Orogen of the Transantarctic Mountains.* Cambridge: Cambridge University Press, 284 pp.

Sutherland, F. L., Hoskin, P. W. O., Fanning, C. M. & Coenraads, R. R. (1998). Models of corundum origin from alkali basalt terrains: a reappraisal. *Contributions to Mineralogy and Petrology* **133**, 356–372.

Talarico, F. & Castelli, D. (1995). Relict granulites in the Ross orogen of northern Victoria Land (Antarctica), I. Field occurrence, petrography and metamorphic evolution. *Precambrian Research* **75**, 141–156.

Talarico, F. M., Palmeri, R. & Ricci, C. A. (2004). Regional metamorphism and P–T evolution of the Ross Orogen in northern Victoria Land (Antarctica): a review. *Periodico di Mineralogica* **73**, special issue 2: a showcase of the Italian research in metamorphic petrology, 185–196.

Tessensohn, F. & Henjes-Kunst, F. (2005). Northern Victoria Land terranes, Antarctica: far-travelled or local products? In: Vaughan, A. P. M., Leat, P. T. & Pankhurst, R. J. (eds) *Terrane Processes at the Margins of Gondwana. Geological Society, London, Special Publications* **2?6**, 275–291.

Tiepolo, M. (2003). *In situ* Pb geochronology of zircon with laser ablation-inductively coupled plasma-sector field mass spectrometry. *Chemical Geology* **199**, 159–177.

Tiepolo, M., Bottazzi, P., Palenzona, M. & Vannucci, R. (2002). A laser probe coupled with ICP-double-focusing sector-field mass spectrometer for *in situ* analysis of geological samples and U–Pb dating of zircon. *Canadian Mineralogist* **41**, 259–272.

Tomaschek, F., Kennedy, A. K., Villa, I. M., Lagos, M. & Ballhaus, C. (2003). Zircons from Syros, Cyclades, Greece—recrystallization and mobilization of zircon during high-pressure metamorphism. *Journal of Petrology* **44**, 1977–2002.

Tonarini, S. & Rocchi, S. (1994). Geochronology of Cambro-Ordovician intrusives in northern Victoria Land; a review. *Terra Antartica* **1**, 46–50.

Tribe, I. R. & D'Lemos, R. S. (1996). Significance of a hiatus in down-temperature fabric development within syntectonic quartz diorite complexes, Channel Islands, UK. *Journal of the Geological Society, London* **153**, 127–138.

Turner, S. P. (1996). Petrogenesis of the late-Delamerian gabbroic complex at Black Hill, South Australia: implications for convective thinning of the lithospheric mantle. *Mineralogy and Petrology* **56**, 51–89.

van Achterbergh, E., Ryan, C., Jackson, S. & Griffin., W. (2001). Appendix 3 Data reduction software for LA-ICP-MS. In: Sylvester, P. (ed.) *Laser-Ablation-ICPMS in the Earth Sciences. Mineralogical Association of Canada, Short Course* **29**, 239–243.

Vavra, G. (1990). On the kinematics of zircon growth and its petrogenetic significance; a cathodoluminescence study. *Contributions to Mineralogy and Petrology* **106**, 90–99.

Vavra, G., Gebauer, D., Schmidt, R. & Compston, W. (1996). Multiple zircon growth and recrystallization during polyphase Late Carboniferous to Triassic metamorphism in granulites of the Ivrea Zone (Southern Alps): an ion microprobe (SHRIMP) study. *Contributions to Mineralogy and Petrology* **122**, 337–358.

Vavra, G., Schmid, R. & Gebauer, D. (1999). Internal morphology, habit and U–Th–Pb microanalysis of amphibolite-to-granulite facies zircons: geochronology of the Ivrea Zone (southern Alps). *Contributions to Mineralogy and Petrology* **134**, 380–404.

Vetter, U. & Tessensohn, F. (1987). S- and I-type granitoids of North Victoria Land, Antarctica, and their inferred geotectonic setting. *Geologische Rundschau* **76**, 233–243.

Vita, G., Lombardo, B. & Giuliani, O. (1991). Ordovician uplift pattern in the Wilson Terrane of the Borchgrevink Coast, Victoria Land

(Antarctica): evidence from K/Ar dating of metamorphic biotites. *Memorie della Societa Geologica Italiana* **46**, 257–265.

Vita, S. G., Feraud, G., Ruffet, G. & Lombardo, B. (1994). K/Ar and ^{40}Ar/^{39}Ar laser-probe ages of metamorphic micas and amphibole of the Wilson Terrane and Dessent Unit, northern Victoria Land (Antarctica): their bearing on the regional post-metamorphic cooling history. *Terra Antartica* **1**, 59–62.

Wayne, D. M. & Sinha, A. K. (1988). Physical and chemical response of zircons to deformation. *Contributions to Mineralogy and Petrology* **98**, 109–121.

Wayne, D. M., Sinha, A. K. & Hewitt, D. A. (1992). Differential response of zircon U–Pb isotopic systematics to metamorphism across a lithologic boundary: an example from the Hope Valley Shear Zone, southeastern Massachussetts, USA. *Contributions to Mineralogy and Petrology* **109**, 408–420.

Whitehouse, M. J. & Kamber, B. S. (2002). On the overabundance of light rare earth elements in terrestrial zircons and its implication for Earth's earliest magmatic differentiation. *Earth and Planetary Science Letters* **204**, 333–346.

Whitehouse, M. J. & Platt, J. P. (2003). Dating high-grade metamorphism: constraints from rare-earth elements in zircon and garnet. *Contributions to Mineralogy and Petrology* **145**, 61–74.

Wysoczanski, R. J. & Allibone, A. H. (2004). Age, correlation, and provenance of the Neoproterozoic Skelton Group, Antarctica: Grenville age detritus on the margin of East Antarctica. *Journal of Geology* **112**, 401–416.

Zeck, H. P. & Whitehouse, M. J. (2002). Repeated age resetting in zircons from Hercynian–Alpine polymetamorphic schists (Betic–Rif tectonic belt, S. Spain)—a U–Th–Pb ione microprobe study. *Chemical Geology* **182**, 275–292.

APPENDIX: SAMPLE CODES AND LOCALITIES OF SELECTED SAMPLES

Abbreviated sample code	Sample code	Locality	Latitude (degrees)	Longitude (degrees)
C1	10/02/88C1	Howard Peaks	−74·281	163·578
M14	18/01/88M14	Howard Peaks	−74·256	163·550
C10	31/01/88C10	NE of Mt. Dickason	−74·361	164·070
C4	31/01/88C4	Mills Peak	−74·253	163·939
DF6	09/12/99DF6A	Tourmaline Plateau	−74·148	163·563
MS1	05/12/93MS1	Tourmaline Plateau	−74·253	163·319
B2	21/01/86B2	Black Ridge	−74·472	163·506
L1	15/01/86L1	Mt. Keinath	−74·541	163·965
DR12	20/12/96DR12	Boomerang Glacier	−74·507	163·778

Selected samples are held at the Earth Science Section of the Museo Nazionale dell'Antartide in Siena (MNA-SI).